Contents lists available at ScienceDirect

Bioactive Materials

Bio-integrated scaffold facilitates large bone regeneration dominated by endochondral ossification

Lili Sun [a,b,1], Haoyi Niu [a,b,e,1], Yuqiong Wu [d], Shiyan Dong [c], Xuefeng Li [c], Betty Y.S. Kim [e], Changsheng Liu [a,b], Yifan Ma [a,c,***], Wen Jiang [c,**], Yuan Yuan [a,b,*]

[a] Key Laboratory for Ultrafine Materials of Ministry of Education, School of Materials Science and Engineering, East China University of Science and Technology, Shanghai, 200237, PR China
[b] Engineering Research Center for Biomedical Materials of Ministry of Education, East China University of Science and Technology, Shanghai, 200237, PR China
[c] Department of Radiation Oncology, MD Anderson Cancer Center, Houston, TX, USA
[d] Department of Prosthodontics, Ninth People's Hospital, Shanghai Jiao Tong University School of Medicine, Shanghai, 200011, PR China
[e] Department of Neurosurgery, The University of Texas MD Anderson Cancer Center, Houston, TX, USA

ARTICLE INFO

ABSTRACT

Repair of large bone defects caused by severe trauma, non-union fractures, or tumor resection remains challenging because of limited regenerative ability. Typically, these defects heal through mixed routines, including intramembranous ossification (IMO) and endochondral ossification (ECO), with ECO considered more efficient. Current strategies to promote large bone healing via ECO are unstable and require high-dose growth factors or complex cell therapy that cause side effects and raise expense while providing only limited benefit. Herein, we report a bio-integrated scaffold capable of initiating an early hypoxia microenvironment with controllable release of low-dose recombinant bone morphogenetic protein-2 (rhBMP-2), aiming to induce ECO-dominated repair. Specifically, we apply a mesoporous structure to accelerate iron chelation, this promoting early chondrogenesis via deferoxamine (DFO)-induced hypoxia-inducible factor-1α (HIF-1α). Through the delicate segmentation of click-crosslinked PEGylated Poly (glycerol sebacate) (PEGS) layers, we achieve programmed release of low-dose rhBMP-2, which can facilitate cartilage-to-bone transformation while reducing side effect risks. We demonstrate this system can strengthen the ECO healing and convert mixed or mixed or IMO-guided routes to ECO-dominated approach in large-size models with clinical relevance. Collectively, these findings demonstrate a biomaterial-based strategy for driving ECO-dominated healing, paving a promising pave towards its clinical use in addressing large bone defects.

Large bone defects associated with traffic accidents and multiple traumas are still a major health problem nowadays. Clinically, today's most accepted gold standard for augmenting bone healing is still bone autograft and the ideal treatment of large bone defects is still missing [1–3]. It is well-acknowledged that insufficient vascularization and limited ability for nutrients or oxygen perfusion are the biggest culprits for osteogenesis failure of the large bone repair [4–6]. Typically, bone defects often heal through mixed routines, including intramembranous

ossification (IMO) and endochondral ossification (ECO). Compared to the IMO process, ECO, which begins with lower metabolic chondrocytes formation and is followed by cartilage hypertrophy and calcification of cartilage template, is not highly dependent on an initial vascular network [7,8]. From this viewpoint, the ECO-guided healing route can be an alternative method for efficient large bone repair. During fetal development, however, most mammalian skeletons, including craniofacial bones, clavicles, and flat bones, often form through mixed or

IMO-dominated routines, revealing that the regular healing process for large bone defects tends to be intrinsically inefficient. Accordingly, we hypothesize that a new approach based on the ECO-enhanced healing process or shifting from a mixed or IMO-dominant to an ECO-dominant healing route, could potentially offer a more attractive and promising strategy to improve repair outcomes when large bone defects occur.

A typical ECO process often undergoes activated chondrogenic differentiation for cartilaginous intermediate and successful bone transformation. Currently, multiple strategies, including biochemical factors, cell sources, and biomaterials, have been employed to recapitulate the route of ECO for improved outcomes of bone regeneration [5,9,10]. Among them, bone morphogenetic protein 2 (BMP-2) as a potent growth factor approved by the Food and Drug Administration (FDA) for clinical use, plays a major part in both chondrogenic and osteogenic lineage commitment of ECO process [10–15]. Notably, the healing routes with BMP-2 have been reported to be associated with physicomechanical environment of the defect sites, which exerts a significant impact on stem cells (e.g., MSCs) differentiation, ultimately determining the mode of fracture healing [16–19]. For example, bone healing with BMP-2 mainly proceeds through ECO route due to the instability of the bone fragments such as those found in long bones, vertebrae, as well as flat bones without rigid stabilization. However, when the mechanical environment at the defect site remains stable (e.g., oral and maxillofacial defect), a combination routes (ECO+IMO) or IMO will predominantly govern the healing process [20–22]. Moreover, studies have demonstrated that BMP-2 can stabilize the ECO process when combined with other growth factors like TGF-β1 or TGF-β3 [23]. However, this stabilization requires supraphysiological dosage of growth factors. For instance, various *in vivo* studies have illustrated that rhBMP-2 significantly speeds up the healing of critical-sized bone defects, like 25 mm segmental canine ulnar defects [24,25]. Yet, these studies involved administering rhBMP-2 at doses exceeding 160 μg. Such high dosages not only raise concerns about cost-effectiveness but also pose potential side effects, including an increased risk of cancer. These findings reveal healing capacity following BMP-2 administration could be unstable and conditional, and thus, an improved therapy based on BMP-2 is essential to ideally recapitulate ECO route in large bone repair. A key contributor in this process is hypoxia-inducible factor-1α (HIF-1α), a transcription
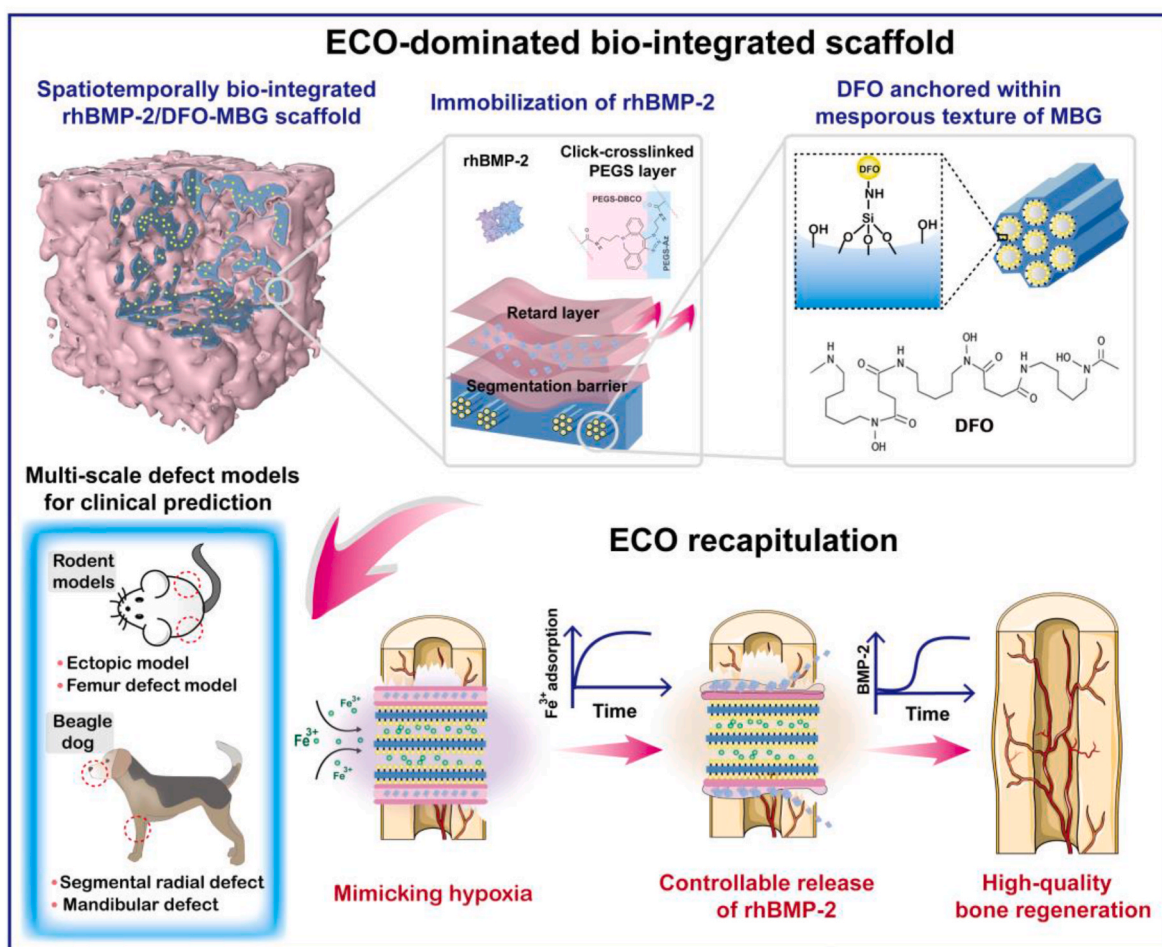
Scheme. 1. | Illustration of the bio-integration of rhBMP-2 and hypoxia-mimicking system for recapitulation of endochondral ossification (ECO)-dominated large bone regeneration. In this system, deferoxamine (DFO) was chemically grafted onto the surface of mesopores within the mesoporous bioactive glass (MBG) scaffold, which could strengthen the localized mass transfer and adsorption of iron ions. Before administering recombinant human bone morphogenetic protein-2 (rhBMP-2), a barrier layer of PEGylated poly (glycerol sebacate) (PEGS), crosslinked via a click reaction, was first incorporated onto the MBG to segregate rhBMP-2 from DFO. Then, rhBMP-2 was entrapped within an additional PEGS layer, which was then coupled with a retarding PEGS layer to facilitate a controllable release profile. This bio-integrated system was applied to multi-scale defect models for mechanism dissection of the ECO-dominated healing process and future clinical prediction. In order to preliminarily explore the functions of each component of bio-integrated scaffolds, mouse ectopic bone formation was applied to evaluate different ECO healing stages, including the early-stage hypoxia-mimicking cartilage formation and the subsequent osteogenesis process. Then, the optimization of ECO-dominated repair through the spatiotemporally arranged administration of low-dose rhBMP-2 and DFO were evaluated in the rat distal femur model. Subsequently, two large animal models (dog mandible defect model and dog segmental radial defect model) were further examined for the bio-integration system, which offered more clinically relevant sizes to address the real-world challenges in large bone defect through an ECO-dominated repair.

factor that regulates crucial genes for cell survival, cartilage formation (such as SOX9, collagen types II and X), and angiogenesis-related genes, particularly within the VEGF pathway, essential for later stages of bone transformation [26]. However, HIF-1α is typically degraded by the ubiquitin-proteasome pathway, mediated by prolyl hydroxylase domain-containing protein 2 (PHD2) in the presence of ferrous ions, α-KG, and oxygen. Inactivation of PHD due to hypoxia, lack of ferrous ions, or α-KG, leads to HIF-1α stabilization and accumulation. Deferoxamine (DFO), as an FDA-approved iron chelator and hypoxia mimicking agent, can activate not only endogenous hypoxia mediated-chondrogenesis by increasing HIF-1α. Based on the rationales above, we believe realizing a well-orchestrated and enhanced ECO process by combining DFO-based mimicking hypoxia and BMP-2 bioactive factor will be a novel strategy with huge clinical significance.

Here, in order to achieve the above purposes, we designed a bio-integrated system to fully and precisely recapitulate the ECO process for large bone regeneration, which formed a hypoxia-mimicking microenvironment immediately in the early stage and then facilitated rapid bone transformation through the BMP-2 pathways. Mesoporous bioactive glass (MBG), a promising biodegradable biomaterial for bone regeneration, was selected as the substrate for the bio-integrated system due to its unique mesoporous structure and functional strut surface [10, 27,28]. These features not merely enable the loading of growth factors like BMP-2 but facilitate surface modification. As illustrated in Scheme 1, DFO is chemically anchored on the MBG scaffold because of a short plasma half-life and high drug toxicity of free DFO, which often leads to severe side effects such as significant hypotension and tachycardia [29]. Previous research has demonstrated the benefits of covalently attaching DFO to substances like dextran, starch, or polyethylene glycol (PEG), which to some extent, reduce its toxicity during delivery [30,31]. Building on this, our study innovatively leverages localized delivery of covalently bound DFO on the MBG scaffold, offering a compelling solution for tissue engineering applications [32–34]. More specifically, the mesoporous structure of the MBG provides a "transportation highway" that can be beneficial to efficient physiological diffusion and chelation of ferrous ions within the mesoporous pores for rapid activation of the localized hypoxia and stability of HIF-1α [35,36]. Then, a biocompatible and biodegradable PEGylated poly (glycerol sebacate) (PEGS) was assembled through a copper-free azide-alkyne click-crosslinked reaction and worked as isolation and recombinant human BMP-2 (rhBMP-2) immobilization layers. In the assembly, rhBMP-2 is supposed to retain high bioactivity with a highly tailorable releasing profile because of the gentle and aqueous-phase synthesis and controllable degradation [37, 38]. Notably, due to the mimicked hypoxia microenvironment and orchestral arrangement, the dosage of rhBMP-2 in this ECO system is predicted to greatly reduce, which avoids the adverse effects caused by the supraphysiological concentration of exogenous growth factor. Aside from the regular demonstration in rodent animals, two large animal models with defects close to the actual clinically relevant sizes, including mandible and segmental radial repairs, were used to further verify the efficiency of this bio-integrated system through the ECO-dominated healing route and its practicability for future clinical application.

1. Results and discussion

1.1. Preparation of a DFO-induced hypoxia-mimicking scaffold with "transportation highway" for rapid activation of localized HIF-1α expression and hypoxia environment

MBG scaffolds were prepared via the sol-gel and polyurethane foam-template methods as described in our previous study [39]. The hierarchically multiporous structure endowed the MBG scaffolds with a high specific surface area for cell or tissue ingrowth as well as drug loading [39]. In consideration of the high toxicity of free DFO, a chemical graft was employed to anchor the DFO on the scaffolds and reduce

immunogenic risk after implantation (Fig. 1A) [31]. Fig. 1B–C and Fig. S2A-C indicate the successful DFO graft on modified-MBG (MBG-CHO) and adjustable iron ion (III) (Fe^{3+}) chelation capacity achieved by mediating the grafting amount with interconnected pore and channel structures unaffected. As a highly specific iron chelator, chelation efficacy and hypoxia degree induced by DFO highly rely on localized irons' incidence. Herein, the MBG scaffold with a mesoporous structure (MBG-T) could offer better mass transfer in physiological dynamic simulation with higher pressure on the flow inlet substrate when compared to MBG without mesoporous structure (MBG-B) (Fig. 1D and Fig. S3A-C), which revealed a higher localized aggregation of Fe^{3+}. Consequently, MBG-T presented a significantly faster ion-chelate kinetic and better chelation capacity than MBG-B (Fig. 1D), thus inducing a more potent and rapid hypoxia effect for the activation of chondrogenic differentiation in the regeneration.

In contrast to the anchored DFO, the other active ingredient rhBMP-2, particularly its bioactivity, is known to be more sensitive to other components, as multiple studies have suggested [40,41]. Given the potential interactions between DFO and rhBMP-2, which probably impair rhBMP-2 activity, preliminary studies were carried out to investigate the osteogenic capacity of rhBMP-2 with the presence of DFO. As shown in Fig. 1F and G, the bioactivity of rhBMP-2 appears to be compromised in both *in vitro* ALP test and *in vivo* ectopic osteogenesis. Further far-ultraviolet circular dichroism spectra (Fig. 1E) showed the secondary structure of rhBMP-2 was shifted when mixed with DFO, indicating that small molecule drugs negatively affected the conformation of growth factors and their bioactivity. These results, for the first time, demonstrate that DFO cannot be in direct combine with rhBMP-2, prompting a delicate segmentation design of two core agents for effective recapitulation of the ECO-based healing process [42,43].

1.2. Delicate construction of a spatiotemporally bio-integrated system administering rhBMP-2 and hypoxia-mimicking MBG-DFO scaffolds through utilizing PEGS hydrogel layers

Hydrogels are commonly used for drug encapsulation and coating because of their excellent biocompatibility and degradability. Among them, PEGS has been widely known for its good biocompatibility, maneuverability, and tailored properties [37,44–48]. Therefore, after stabilizing DFO on the MBG scaffolds (DFO-MBG), a biodegradable PEGS layer was synthesized via a copper-free azide-alkyne click-crosslinked reaction (Fig. 2A). This allowed for the assembly of DFO-MBG and rhBMP-2 with spatiotemporal profiles. The results from ^{1}HNMR and Fourier-transform infrared (FT-IR) spectra demonstrate the successful synthesis of modified-PEGS derivatives for subsequent click chemistry (Fig. 2B). As shown in Fig. 2C, rapid gelation occurred, resulting in the formation of a hydrogel after mixing the PEGS-DBCO and PEGS-AZ precursor solutions. Herein, the degree of crosslinking and the biodegradability of PEGS, which could be precisely regulated by the ratios of functional groups within the polymer derivatives (Fig. 2D), were leveraged to establish improved ECO-based regeneration in different animal models (Table 2) through optimization of the spatiotemporal dosage of the incorporated growth factors. At the same time, we confirmed by far-ultraviolet circular dichroism spectra (Fig. 2E) that rhBMP-2 released from PEGS could maintain its conformation and bioactivity.

Via the preparation of DFO-MBG and modified-PEGS derivatives, we further designed a spatiotemporally integrated system. This system is specifically tailored to facilitate each phase of the ECO process, including the early stage of hypoxia-mimicking chondrogenic differentiation and the late stage of bone transformation, thereby enhancing the overall osteogenic outcomes. The bio-integrated scaffolds designed for different purposes in the study were shown in Fig. S1. Specifically, rhBMP-2 was introduced into the PEGS hydrogel to prepare rhBMP-2-loaded layer, which was further separated from the MBG-DFO substrate by a blank PEGS barrier layer to achieve the spatiotemporal bio-
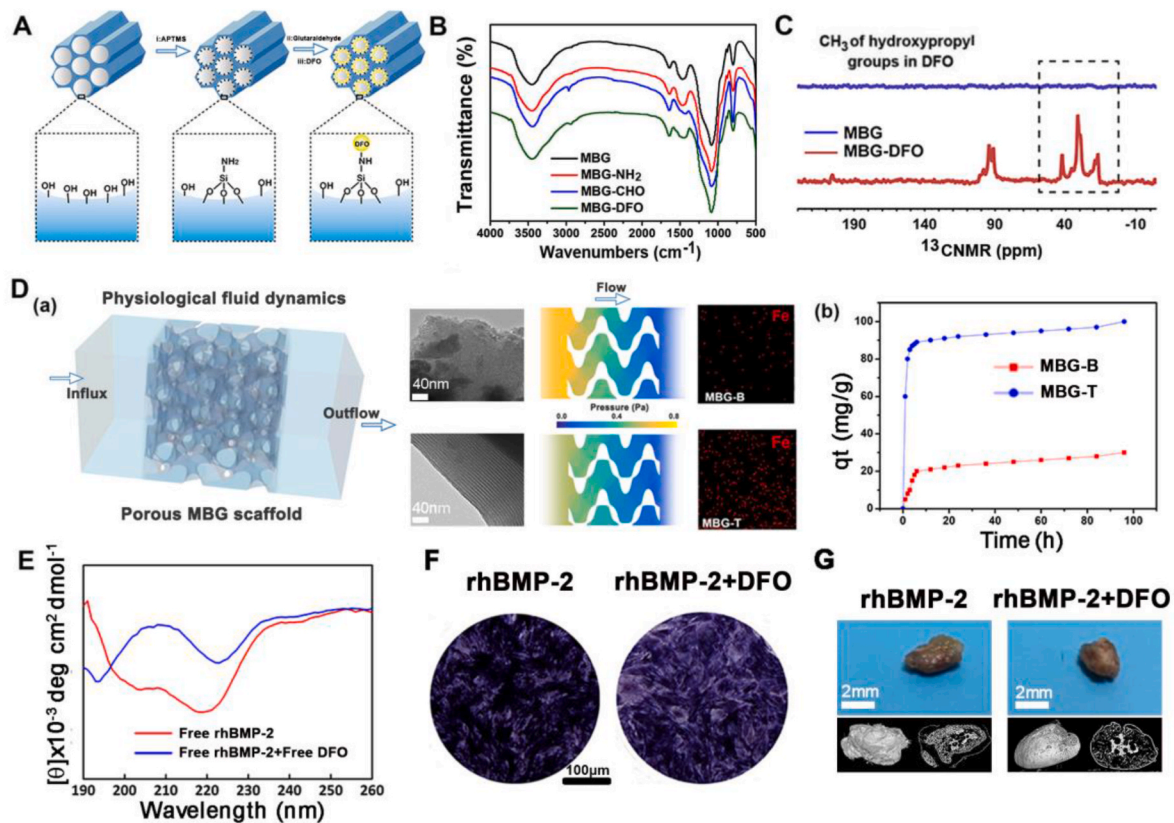
Fig. 1. │ Preparation of a DFO-induced hypoxia-mimicking scaffold with "transportation highway" for rapid activation of localized HIF-1α expression and hypoxia environment. A, Illustration of the MBG-DFO synthesis process. Characterization of the MBG-DFO scaffold: **B,** FTIR spectra of the MBG, synthetic intermediate (MBG-NH$_2$ and MBG-CHO) and MBG-DFO scaffolds. The spectra feature a peak in the 2800-3050 cm^{-1} range, representing the stretching vibration peak of C–H and C–C, suggesting successful grafting of DFO. **C,**^{13}CNMR spectra of the MBG and MBG-DFO scaffolds. The chemical shift δ peak at 22.6 ppm, which can be attributed to the −CH$_3$ portion of MBG-DFO, provides further evidence for the successful grafting of DFO. **D,** The chelation activity of iron ions (III) (Fe^{3+}) by MBG-B and MBG-T simulated by mass transfer model and further confirmed through Energy-dispersive X-ray spectroscopy (EDS) and Inductively coupled plasma (ICP) analysis. (a) Mass transfer model for the simulation of physiological fluid dynamic in different MBG scaffolds (MBG without mesoporous structure (MBG-B) and MBG with mesoporous structure (MBG-T)). According to the section plane, the inlet pressure of MBG-T (0.577 Pa) is significantly lower than that of MBG-B (0.888 Pa), which indicates MBG-T has stronger mass transfer than MBG-B. (b) Dynamic of Fe^{3+} chelation detected by ICP. MBG-T demonstrated a significantly more robust Fe^{3+} adsorption capability compared to MBG-B. **E,** Far-ultraviolet circular dichroism spectra of rhBMP-2 when exposed to DFO. Changes in the secondary structures of rhBMP-2 can be found upon the introduction of DFO, potentially leading to adverse effects on the growth factor's bioactivity. **F,** Alkaline phosphatase (ALP) staining of rat bone marrow mesenchymal stem cells (rBMSCs) with single rhBMP-2 and combination of rhBMP-2 and DFO (rhBMP-2+DFO) for 7 days. More intensive ALP staining effect (deeper purple) can be observed in single rhBMP-2 group when compared to rhBMP-2+DFO, suggesting that direct combination could affect bioactivity of rhBMP-2 for osteogenic differentiation. **G,** Digital photographs and micro-computed tomography (Micro-CT) images of ectopic bone formation after 4-week implantation. The relative new bone volume fraction (BV/TV) of the group with single rhBMP-2 loaded on the MBG scaffold was 7.22 ± 0.426 %, while the group with direct combination of rhBMP-2 and DFO within the MBG scaffold exhibited a BV/TV of 5.07 ± 0.568 %.

integration of rhBMP-2 and DFO (Fig. 2F). The outer surface of the scaffolds was then coated with another PEGS layer for the delayed release of rhBMP-2 (Fig. 2F). This spatiotemporally bio-integrated system is designated as the D@M+B@P scaffold. Fig. S4 illustrates the uniform distribution of rhBMP-2 within the PEGS hydrogels applied to the MBG scaffolds, suggesting the effective dispersal of the protein in the bio-integrated scaffold. The integration of PEGS hydrogel layers resulted in a noticeable colour shift in the scaffold's appearance (Fig. 2G), yet the pore size of these bio-integrated scaffolds consistently remained within the approximate range of 200–500 μm (Fig. 2I). These findings, along with those presented in Fig. S2B, demonstrate that the incorporation of the PEGS layer into the spatiotemporally bio-integrated scaffold does not compromise the interconnected porous structure and the mesoporous channels, as well as the binding capacity for Fe^{3+}. Moreover, the incorporation of PEGS coating layer significantly enhanced the compressive strength of the MBG scaffold (Fig. S5). Regarding the degradation profile (Fig. S6), the bio-integrated scaffolds with incorporated PEGS layers showed a notably faster degradation rate in the initial phase compared to the MBG scaffold, which could be attributed to

faster degradation properties of the PEGS relative to the MBG substrate. Further protein release profiles, as shown in Fig. 2H, indicate that a controllable and sustained release of rhBMP-2 can be achieved in the scaffold with the PEGS layer (e.g., the degree of crosslinking is 80 %), where the main release started after 7 days and cumulative release can last for over 30 days. In this system, the desirable mobility of the pre-PEGS derivative aqueous solution and the rapid and gentle cross-linking reaction strongly contributed to the successful assembly outcomes and controllable release profiles while retaining the bioactivity of the growth factor [37,49].

1.3. The spatiotemporally bio-integrated rhBMP-2/DFO-MBG scaffold enhances the early stage of ECO

Microenvironmental factors often participate in critical biological processes and affect biological signalling pathways. Among these pathways, HIF-1α is the key effector of low O$_2$ sensing during cellular adaptation. In the last section, we successfully demonstrated the effective anchoring of DFO onto multiporous MBG scaffolds, ensuring a high
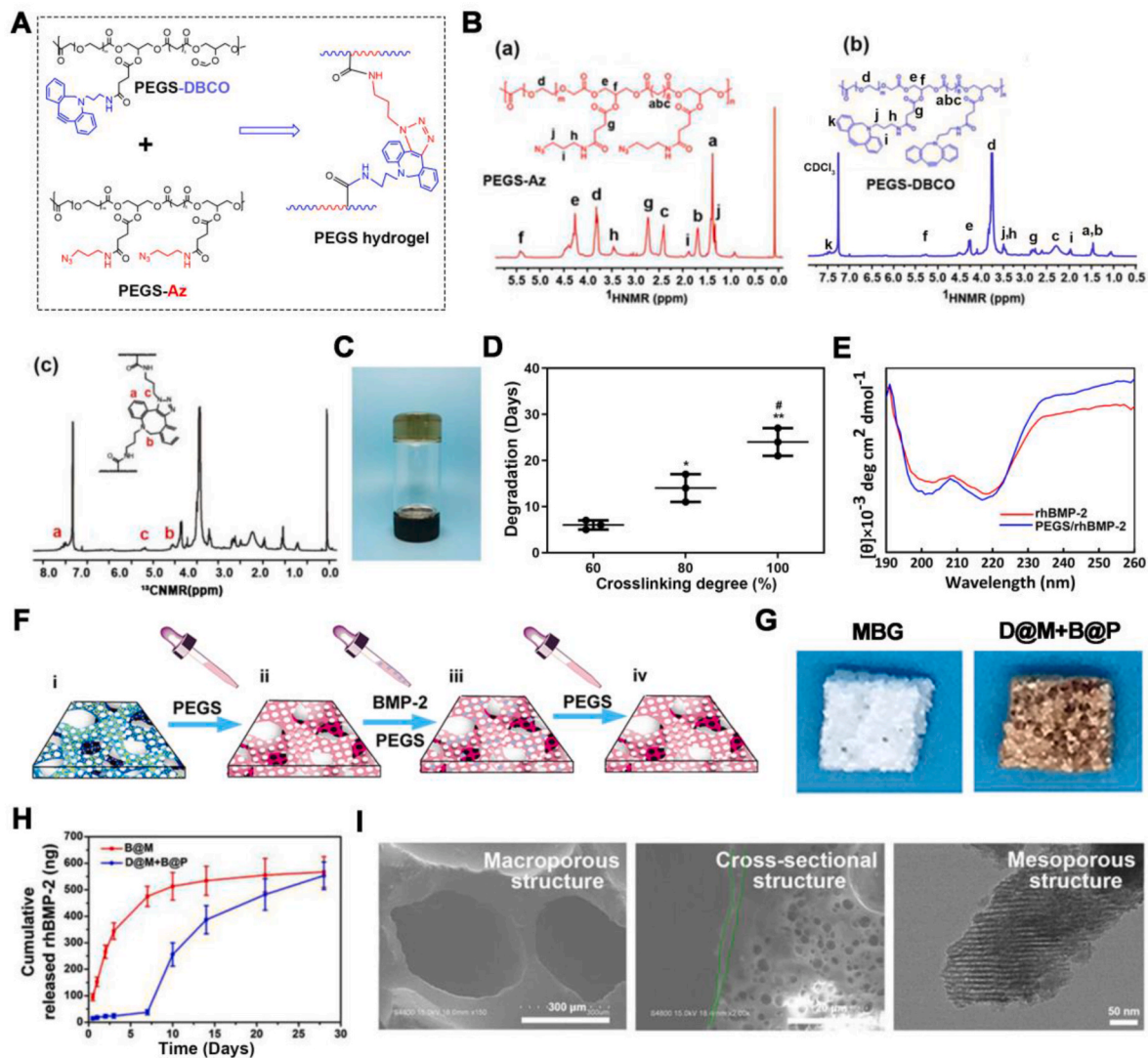
Fig. 2. | Delicate construction of a spatiotemporally bio-integrated system administering rhBMP-2 and hypoxia-mimicking MBG-DFO scaffolds through utilizing PEGS hydrogel layers. A, PEGS hydrogel preparation through a copper-free azide-alkyne click-crosslinked reaction. **B,** Characterization of the PEGS polymer and hydrogel. ^{1}HNMR spectra of (a) PEGS-Az and (b) PEGS-DBCO, and ^{13}CNMR spectra of (c) PEGS hydrogel. For PEGS-Az, the presence of peaks marked as i, j and h at δ 1.91 ppm, δ 1.30 ppm, and δ 3.45 ppm provide evidence for the successful grafting of the azide group. For PEGS-DBCO, the peaks marked as i, j, h and k at 1.95 ppm, δ 3.53 ppm, δ 3.40 ppm and δ 7.45 ppm provide evidence for the successful grafting of the DBCO moiety. **C,** Visual characteristics of the PEGS hydrogel. **D,** *In vitro* degradation profile of the PEGS hydrogel with different crosslinking degree. (n = 3) **E,** Far-ultraviolet circular dichroism spectra of rhBMP-2 released from PEGS hydrogel layer. The secondary structure of released rhBMP-2 was similar to that of the free one, suggesting that PEGS administration did not negatively impact the bioactivity of the growth factor. **F,** Schematics of the preparation protocol for spatiotemporally bio-integrated system administering rhBMP-2 and hypoxia-mimicking MBG-DFO scaffolds through utilizing PEGS hydrogel layers. This spatiotemporal bio-integrated system is referred to as the D@M+B@P scaffold. As control groups, two kind of scaffolds were prepared that either directly combined rhBMP-2 with DFO-MBG (named (D+B)@P), or loaded rhBMP-2 solely onto the MBG substrate (named B@M). **G,** The digital photos of MBG and D@M+B@P scaffolds. **H,** *In vitro* release kinetics of rhBMP-2 from B@M and D@M+B@P at a fixed immobilization amount (1 μg). **I,** Structural observation of the prepared D@M+B@P scaffold. SEM images: macroporous networks (Scale bar: 300 μm) and cross-sectional structure (Scale bar: 20 μm); TEM image: mesoporous structure (50 nm). Green lines represent the coated PGES hydrogel layers on the D@M+B@P scaffold. The thickness of the PEGS layers was approximately 2 μm. Asterisk '*' refers to statistical significance when compared 60 % crosslinking degree, while Pound '#' refers to the statistical significance when compared to 80 % crosslinking degree. *,#p < 0.05, **p < 0.01. All data were presented as mean ± SD. One-way ANOVA followed by Tukey's post hoc tests was used for comparison.

payload and uncompromised chelation capability. Then, the initiation of an early-stage, hypoxia-mimicking microenvironment and cell recruitment, facilitated by the spatiotemporally bio-integrated scaffold were assessed using a rat distal femur defect model (Fig. 3A). As shown in Fig. 3B, HIF-1α protein expression is significantly increased in scaffolds modified with DFO compared to scaffolds without DFO modification, and reciprocally, there is a lower prolyl hydroxylase domain (PHD) protein expression in scaffolds without DFO modification. Intuitively, the group with a direct combination of rhBMP-2 and DFO-MBG ((D+B) @P) and the spatiotemporally arranged group (D@M+B@P) showed higher expression and more significant nuclear aggregation of HIF-1α in the rat bone marrow stromal cells (rBMSCs) when compared to the single rhBMP-2 group (B@M) (Fig. 3C–E). To explore the *in vivo* activation of mimicked hypoxia, the tissues and cells within the implanted scaffolds were immunostained after being collected from rat distal femur defects at 3 days post-operation. As anticipated, intensive HIF-1α expression could be found in both D@M+B@P and (D+B) @P cohorts but not in the B@M group (Fig. 3D–F), which suggested potent activation of a hypoxia-mimicking pathway through the DFO chelation against Fe^{3+} *in vivo*. By mimicking the hypoxic microenvironment, recruitment

Table 1

Abbreviation and related information of bio-integrated scaffolds used in the enhanced recapitulation of endochondral ossification (ECO).

Abbreviation	Expanded statement
DFO	Deferoxamine
PEGS	PEGylated poly (glycerol sebacate)
HIF-1α	Hypoxia-inducible factor-1α
RhBMP-2	Recombinant human bone morphogenetic protein 2
MBG	Mesoporous bioactive glass
D@M	DFO grafted MBG
B@M	rhBMP-2 loaded MBG
(D+B)@P	Direct combination of rhBMP-2 and DFO
D@M+B@P	Spatiotemporal bio-integration of rhBMP-2 and DFO
IMO	Intramembranous ossification
ECO	Endochondral ossification

could be facilitated by activating the expression of SDF-1α, which is known as a downstream target of the HIF-1α pathway and could further guide early bone regeneration. Accordingly, the effect of the scaffolds on rBMSC recruitment was explored *in vivo* via dual-staining for CD44 and CD90 markers at 3-day post-operation (Fig. 3D). These results indicate an apparent increase in the recruitment of rBMSCs of the D@M+B@P group. To further investigate the effects of mimicking the hypoxic microenvironment on cell migration, the scaffolds collected from the rat distal femur defect sites after 3-day surgery were then cocultured with rBMSCs in a Transwell® system. Compared to B@M, both (D+B) @P and D@M+B@P groups were found to significantly promote the *in vitro* migration of rBMSCs (Fig. 3G–H).

ECO is the primary route for repairing large bone defects, and its early key processes include cartilage formation and hypertrophy. There are similarities in the early regenerative events of ECO between ectopic and orthotopic models, and therefore, the ectopic bone formation process was first explored to investigate the influence and functionality of the spatiotemporal bio-integrated system on the early ECO steps. At the stage of chondrogenic differentiation, multiple studies have shown that HIF-1α is an essential factor in the early mimicking of hypoxia, maintaining chondrocyte homeostasis and differentiation [15,50,51]. Herein, we explored the effects of B@M, (D+B) @P and D@M+B@P scaffolds on chondrogenic differentiation and hypertrophy via gene microarrays and protein expression analysis of chondrogenesis-related and hypertrophy-related markers, and histological and immunohistochemical (IHC) staining of ectopic bone sections after 3 days of *in vivo* implantation (Fig. 4A). As shown in Fig. 4B, D@M+B@P induces a remarkable increase in the expression of both Col 2a1 and SOX 9 genes. On the other hand, (D+B) @P, despite not enhancing expression to the same extent as the D@M+B@P group, also shows significantly increased expression of Col 2a1 compared to B@M. The protein expression findings were similar to the gene expression results. Notably, the D@M+B@P scaffolds significantly elevated the expression of SOX9 on day 3 compared to both the (D+B) @P and B@M groups (Fig. 4D). Histological/IHC observations and quantification analyses further

demonstrated superior formation of cartilage matrix (Safranin O/Fast Green (SO), Alcian Blue, Masson's Trichrome (MT) and Col II staining) by chondrocytes in the D@M+B@P groups compared to those in the (D+B) @P and B@M groups after 3 days of *in vivo* implantation (Fig. 4C–E). D@M+B@P groups also showed the highest expression of Col X matrix with a relative low level of Col I matrix (Fig. 4C–F, G). These findings suggest that the hypoxic microenvironment, induced by DFO, significantly enhances chondrogenic differentiation in the spatiotemporally bio-integrated scaffolds. Additionally, the cells on the D@M+B@P scaffolds exhibited higher expression of hypertrophic markers (Col X) compared to the B@M groups (Fig. 4C, D, F), revealing a more efficient transition towards cartilage hypertrophy, thereby promoting new bone ingrowth within the D@M+B@P groups. The effects of the D@M+B@P groups on the later events of ECO were further validated in the ensuing *in vivo* experiments.

To gain a more comprehensive understanding of the spatiotemporally bio-integrated system across various stages of the ECO process, we then analyzed the gene expression of tissues surrounding the B@M and D@M+B@P scaffolds through mRNA-seq (Fig. 4H). Based on the analysis of differential genes, the top 10 regeneration-related KEGG pathways were identified, including focal adhesion, osteoclast differentiation, PI3k-AKT signaling pathway, MAPK signaling pathway, VEGF signaling pathway, Hedgehog signaling pathway and etc. Upon constructing the KEGG pathway network, we found that the Hedgehog signaling pathway served as a key initiator, triggering the downstream pathways integral to the early stages of the ECO healing process, particularly the Wnt signaling pathway. Notably, both the (D+B) @P and D@M+B@P groups displayed significantly increased expression levels of Wnt5a and Wnt11 in the noncanonical Wnt signaling pathway. As previous studies have suggested, Wnt5a primarily enhanced the signal transduction of TGF-β for cartilage development, and in this work, Wnt5a caused by the activated hypoxia signaling pathway contributed to more robust cartilage-related signal transduction and chondrogenic differentiation [52]. In addition, the nonclassical Wnt-flt signaling pathway often negatively regulates the angiogenesis induced by the VEGF pathway, which could impair early healing via the IMO route [53]. In contrast, HIF-1α-mediated ECO remains effective as it creates a cartilage intermediate during the early stage, which is featured in avascular tissue with low dependence on the VEGF pathway.

Many studies have demonstrated that hypoxic conditions during the early healing cascade are associated with sufficient chondrogenesis and thus lead to successful healing outcomes. Insufficient chondrogenesis, conversely, could lead to imbalanced regeneration. Based on the transcriptome sequencing results, we further analyzed the expression of key proteins involved in regulating cartilage-related pathways. As shown in Fig. 4I, cartilage differentiation and maturity proteins, such as Indian hedgehog homolog (Ihh) and Wnt 5a were significantly upregulated in the (D+B) @P and D@M+B@P groups when compared to the B@M group, with D@M+B@P exhibiting the highest degree of upregulation. A similar trend of upregulation was observed in cartilage-related extracellular matrix proteins, including Col II and Col X. It is well-

Table 2

| Parameters of scaffolds and design purposes for different animal models.

Animal models	Scaffold size	Parameters of PEGS layer	rhBMP-2 amount (μg)	DFO grafting amount (μmol)	Implantation timeline	Main study purposes
Ectopic bone formation	Cylinder (φ 2.5 mm × 5 mm)	10μl, 60 % crosslinking degree	5	0.124 ± 0.02	3, 7 and 14 days	Functional exploration of bio-integrated scaffolds in different ECO healing stages
Rat distal femur defect	Cylinder (φ 2.5 mm × 5 mm)	10μl, 80 % crosslinking degree	10 (high)/1 (low)	0.124 ± 0.02	3 days/2, 4 and 8 weeks	Optimization of ECO-dominated repair through the spatiotemporally arranged administration of low-dose rhBMP-2 and DFO
Beagle dog segmental radial defect	Cylinder (φ 7 mm × 20 mm)	250μl,100 % crosslinking degree	20	4.76 ± 0.94	4 and12 weeks	Pre-clinical validation of enhanced ECO-dominated large bone repair
Beagle dog mandibular defect	Cuboid (10 mm × 5 mm × 5 mm)	250μl, 100 % crosslinking degree	10	1.86 ± 0.37	4 and 12 weeks	Pre-clinical validation of transition from an IMO-guided repair towards an ECO-dominated repair route
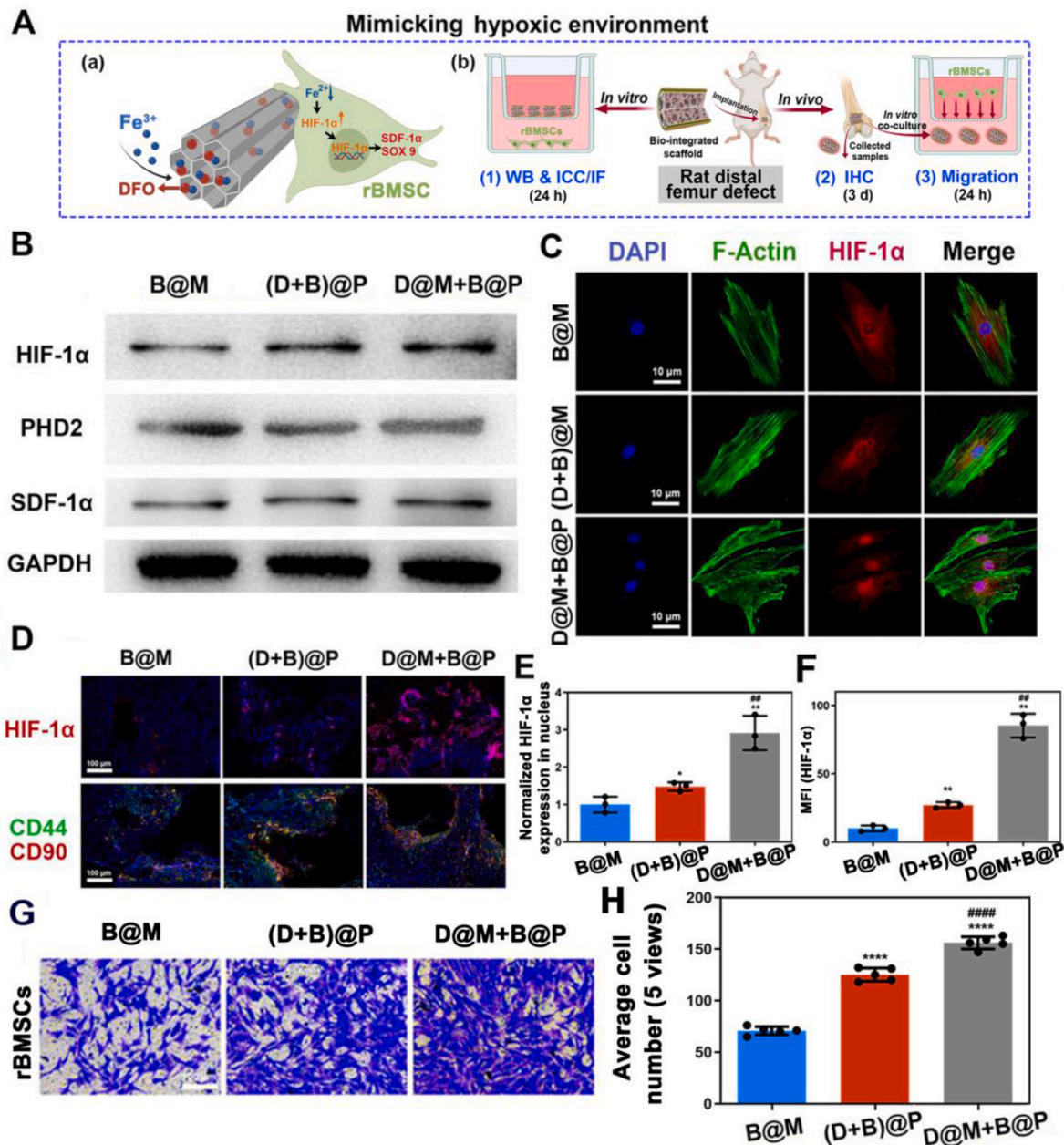
Fig. 3. | The spatiotemporally bio-integrated rhBMP-2/DFO-MBG scaffold enhances mimicking of hypoxic microenvironment and cell recruitment in the early stage of ECO. A, Schematics of the experimental process and timeline demonstrating the initiation of an early-stage, hypoxia-mimicking microenvironment and cell recruitment, facilitated by the bio-integrated scaffold, in a rat distal femur defect model. (a) The chelation of iron ions by the DFO anchored within the bio-integrated scaffold induced the activation of the HIF-1α signaling pathway. (b) Proposed *in vitro* and *in vivo* experiments and timeline in the rat distal femur defect model. **B,** Western blot analysis of HIF-1α, PHD2 and SDF-1α expression in rBMSCs co-cultured with the rhBMP-2/DFO-MBG scaffolds for 24 h. **C,** The aggregation of HIF-1α in the nucleus of rBMSCs detected by Immunocytochemistry (ICC)/Immunofluorescence (IF) staining in 24 h (Scale bar: 10 μm) **D,** Tissue and cells within the rhBMP-2/DFO-MBG scaffolds immunostained by antibodies against HIF-1α (pink), CD44 (green), and CD90 (red) to identify *in vivo* HIF-1α expression and rBMSCs recruitment after 3-day implantation. Cell nuclei were stained with DAPI (blue). **E,** Quantitative analysis of HIF-1a expression in nucleus detected by ICC/IF from **(C).** (n = 3) **F,** Quantitative analysis of mean fluorescence intensity (MFI) reflecting HIF-1α expression determined by Immunohistochemistry (IHC) from **(D).** (n = 3) **G,** The 24-h migration assay of rBMSCs using Transwell® after co-culture with extracted samples from rat distal femur defects three days post-implantation. **H,** Quantitative analysis of migrated rBMSCs. (n = 5). Asterisk '*' refers to statistical significance when compared to B@M, while Pound '#' refers to the statistical significance when compared to (D+B)@P. *p < 0.05, **, ##p < 0.01, ****, ####p < 0.0001. All data were presented as mean ± SD. One-way ANOVA followed by Tukey's post hoc tests was used for comparison.

known that Ihh and Wnt signaling pathways derived from prehypertrophic chondrocytes play a significant role in regulating chondrocyte maturation [54,55]. When the HIF-1α expression was inhibited, there was a significant downregulation of these related proteins in the (D+B) @P and D@M+B@P groups, but not in the B@M group. This observation confirmed the crucial role of HIF-1α during the early stages of ECO

in augmenting chondrogenic differentiation and functional maturation through this bio-integrated rhBMP-2/DFO-MBG system.
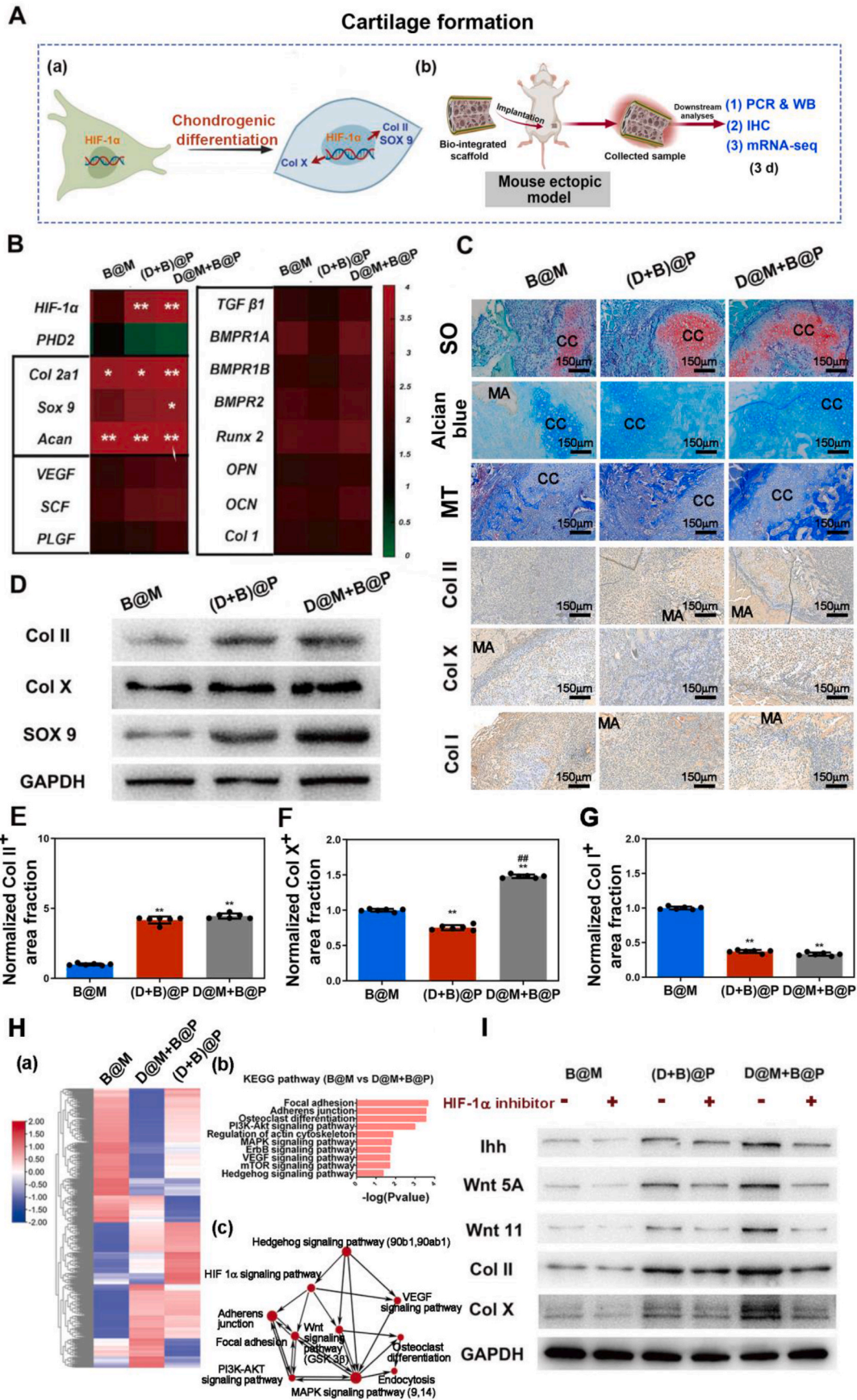
Fig. 4. | The bio-integrated rhBMP-2/DFO-MBG scaffold augments early chondrogenic differentiation and cartilage formation by activating Hedgehog (Hh) signaling pathway in a mouse ectopic bone formation model. A, Schematics of cartilage formation facilitated by the bio-integrated scaffold in a mouse ectopic bone formation model. (a) Chondrogenic differentiation through the activation of the HIF-1α pathway and its downstream pathways. (b) Proposed downstream analyses performed post-3-day implantation in the mouse ectopic bone formation model. **B,** Microarray analysis of crucial gene markers associated with chondrogenic differentiation in tissues and cells harvested from rhBMP-2/DFO-MBG scaffolds post 3-day implantation. **C,** Histological evaluation and IHC staining of ectopic bone tissue sections harvested after a 3-day post-implantation, using Safranin O/Fast Green (SO), Alcian Blue, Masson's Trichrome (MT) staining along with Col II, Col X and Col I. CC: Chondrocyte, MA: Material residues. (Scale bar: 150 μm) **D,** Western blot analysis of protein expression levels of Col II, Col X, and SOX9 in tissues and cells collected from samples after 3 days of *in vivo* implantation. **E-G.** Quantitative analyses of **(E)** Col II-positive, **(F)** Col X-positive and **(G)** Col I-positive cells based on the results from IHC staining of ectopic bone tissue. (n = 6) **H,** RNA-sequence analysis of tissues and cells obtained from the ectopic bone after a 3-day post-implantation. (a) Heatmaps of differentially expressed genes in the D@M+B@P, (D+B) @P and B@M groups. In all differentially expressed mRNAs, |log2 ratio|>1 and Q value < 0.05 were identified as statistically significant. Among them, 1080 upregulated genes and 1310 downregulated genes were observed in the D@M+B@P group when compared to the B@M group. (b) Top 10 regeneration-related KEGG pathway enrichments in D@M+B@P as compared to B@M. (c) Predicted pathway connection based on the KEGG pathway enrichment. **I,** Western blot analysis of typical signal pathways associated with chondrogenic differentiation (Ihh, Wnt 5A, Wnt 11, Col II and Col X) under regulation of an HIF-1 inhibitor (LW6, 20 μM) for 24h. Asterisk '*' refers to statistical significance when compared to B@M, while Pound '#' refers to the statistical significance when compared to (D+B)@P. **, ##p < 0.01. All data were presented as mean ± SD. One-way ANOVA followed by Tukey's post hoc tests was used for comparison.

1.4. Enhanced osteogenesis and angiogenesis of the spatiotemporally bio-integrated system in the late stage of ECO recapitulation

Next, we explored the effect of the spatiotemporally bio-integrated rhBMP-2/DFO-MBG system on the formation of blood vessels and mineralized bone in a later stage of ECO recapitulation (Fig. 5A). As shown in Fig. 5B, the D@M+B@P group exhibited a significant increase in VEGF and RUNX2 gene expression compared to that of the B@M and (D+B) @P groups. Likewise, D@M+B@P significantly increased the expression of Col I matrix after 14 days compared with that in the (D+B) @P and B@M groups (Fig. 5C). However, there was less Col II matrix existed in D@M+B@P (Fig. 5C and D). Additionally, the cells and tissues within the D@M+B@P scaffolds showed increased expression of vascular markers (CD31) (Fig. 5C–E) and more medullary cavity (Fig. 5C–F) compared with these of the other groups from histological/IHC observation and quantification analyses. Ossification/angiogenesis-related proteins were further analyzed by Western blot in all groups (Fig. 5G), and the expressions of VEGF, Col I and OCN were found upregulated most profoundly in the D@M+B@P group compared to the other groups.

The Wnt/β-catenin (or "canonical" Wnt) signaling pathway is known to govern a myriad of biological processes underlying the development and maintenance of tissue homeostasis. During bone development, conditional activation of the Wnt/β-catenin signaling pathway leads to osteoblast differentiation and bone formation [56]. As shown in Fig. 5H, when the BMP-2 pathway was inhibited, the expression of downstream proteins including GSK3β, Col I, OCN, and β-catenin, was correspondingly decreased, which indicated that rhBMP-2 in the bio-integrated system was the head agent for regulating later ossification during the ECO recapitulation. These findings further highlight the significance of rhBMP-2 bioactivity in the later stages of ECO, and suggest the necessity of a spatiotemporally bio-integration of rhBMP-2 and DFO-MBG to circumvent potential adverse interactions.

1.5. Improved ECO-based regenerative outcomes in rat critical-size femoral defects obtained from spatiotemporally bio-integration and low-dose rhBMP-2

After dissecting the bio-integrated scaffolds at each ECO step, we further evaluated the ultimate regenerative outcomes in critical-size defects created at the distal femur heads (Fig. 6A). In the preliminary studies, we found (D+B) @P group induced significantly less bone formation than D@M+B@P cohort, even less than the B@M in the ectopic bone models (Fig. S7). Similar results were observed in the distal femur model. Micro-CT analysis at different time points (Fig. 6C–E) showed that the (D+B) @P group exhibited the poorest regenerative outcomes except at week 2, whereas D@M+B@M demonstrated the best regeneration throughout all periods. Further IHC analyses were further performed for identify the presence of abundant functional cells and tissues

within the defect sites, including osteoblast lineage cells (Col I-positive cells), chondrocytes (Col II-positive cells), and hypertrophic chondrocytes (Col X-positive cells). As shown in Fig. 6F–I and Fig. S10, the tissues in B@M exhibited only weak Col II expression in the early weeks, while the tissues in the (D+B) @P and D@M+B@P groups showed significantly higher expression of Col II, indicating early aggregation of chondrocytes at the defect sites after implantation of rhBMP-2/DFO scaffolds, which could be attributed to the hypoxia-mimicking environment induced by DFO. At 8 weeks, the D@M+B@P group showed the highest expression of Col I and the lowest Col ll and Col X, indicating favorable ossification due to the spatiotemporal bio-integration of rhBMP-2 and DFO. In contrast, the (D+B) @P group still showed high expression of CoI II and the lowest expression of Col I, even lower than that in B@M group, which suggested that DFO could impair the bioactivity of rhBMP-2 and thus require spatiotemporal arrangement. Moreover, osteoclast quantification was performed at week 8 through tartrate-resistant acid phosphatase (TRAP) staining (Fig. S9), which is highly associated with the degradation of grafted material or and the increase in new bone formation. The results indicated that the D@M+B@P group exhibited the lowest fraction of TRAP-positive area, while the (D+B) @P group showed the highest level, suggesting that in the D@M+B@P group, most of the grafted substrate has been converted into new bone structure within the defects, leading to improved bone regeneration. All these findings suggest directly immobilizing rhBMP-2 on the DFO-MBG scaffold resulted in undesirable regenerative effects. This can be attributed to the negative effects of DFO on the bioactivity of exogenous rhBMP-2 due to the change in protein structures (Fig. 1E) or loading conditions (i.e., pH value and ion concentration) [57,58]. Therefore, the spatiotemporal integration of rhBMP-2 and DFO-MBG is indispensable for effectively recapitulating the ECO process and obtaining a high-quality bone repair.

BMP-2 is considered a potent osteogenic growth factor to promote chondrocyte hypertrophy and bone mineralization, thus driving the endochondral bone formation and addressing inadequate chondrocyte hypertrophy in the regular ECO-based regeneration [59]. However, BMP-2 is often delivered at supraphysiological doses with a high incidence of burst release, which has been associated with many complications, particularly heterotopic ossification (HO), which often leads to tissue impingement, secondary fracture, and the possible occurrence of malignant transformation to osteosarcoma [60–62]. In this study, the as-prepared spatiotemporally bio-integrated system was designed with a series of PEGS layers for the controllable release of rhBMP-2. Moreover, we found that the dosage of rhBMP-2 in the system could be reduced to only 1/10 of the dosage in clinical use and mitigate the adverse effects of exogenous growth factors to a large extent. As shown in Fig. 6B, severe HO occurred when a clinical rhBMP-2 dose (10 μg) was applied in the distal femur model, while the complications associated with supraphysiological concentrations were eliminated when the rhBMP-2 dose was lowered to 1 μg, without impairing regeneration efficacy. The
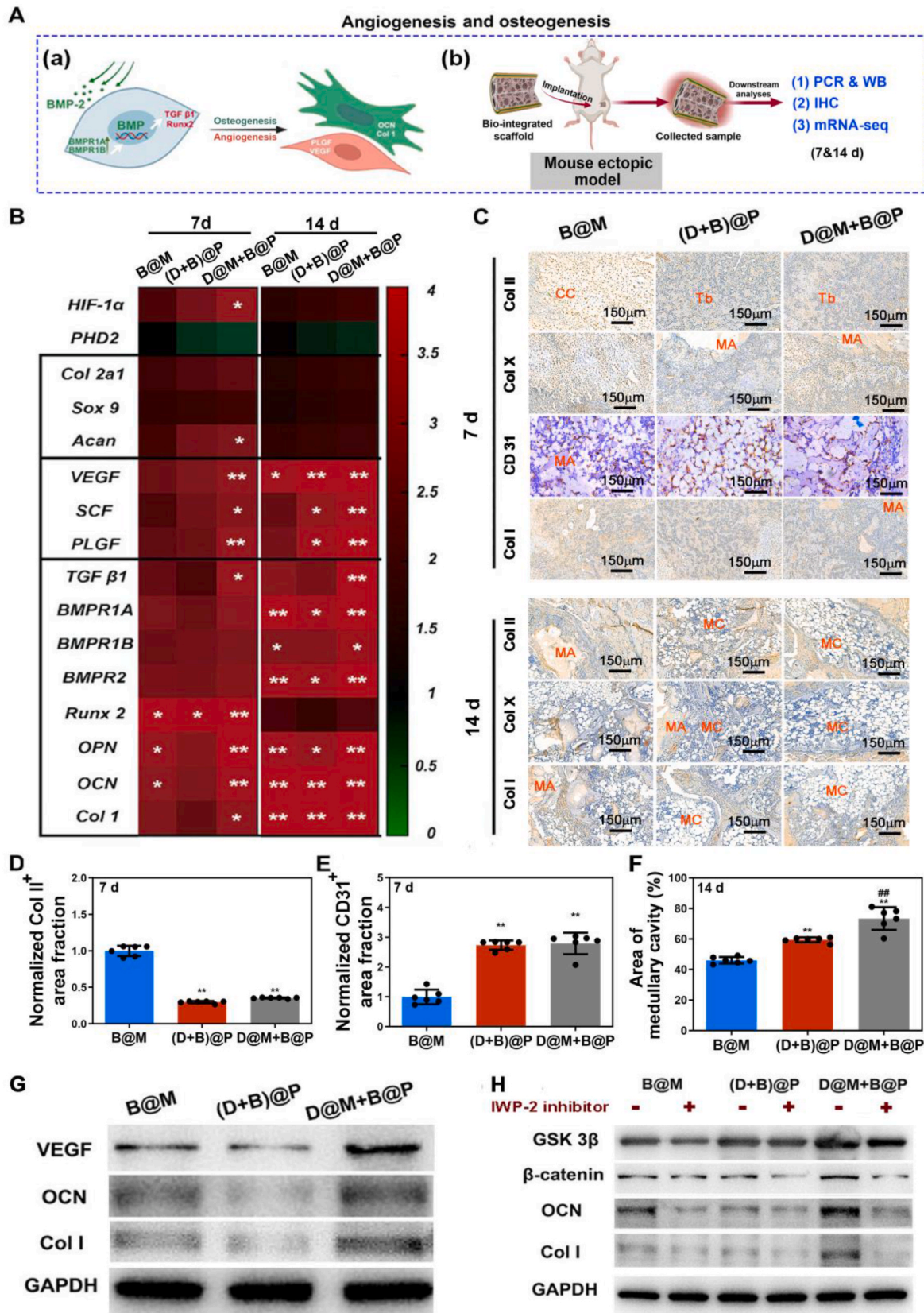
(caption on next page)

Fig. 5. | The bio-integrated rhBMP-2/DFO-MBG scaffold enhances both osteogenesis and angiogenesis during the late stage of ECO in a mouse ectopic bone formation model. A, Schematics of cartilage formation facilitated by the bio-integrated scaffold in a mouse ectopic bone formation model. (a) Enhanced osteogenesis and angiogenesis during the late stage of ECO through the activation of BMP-2 pathway. (b) Proposed downstream analyses performed after 7-day and 14-day implantation in the mouse ectopic bone formation model. **B,** Microarray analysis of crucial gene markers associated with angiogenic and osteogenic differentiation in tissues and cells harvested from rhBMP-2/DFO-MBG scaffolds post 7-day and 14-day implantation. **C,** IHC staining of ectopic bone sections harvested after a 7-day and 14-day post-implantation with stain of Col II, Col X, Col I and CD31. Brown color staining indicates compatibility of antibody against targeted antigen. CC: Chondrocyte, MA: Material residues, MC: Marrow cavity, Tb: Trabecula bone. (Scale bar: 150 μm) **D-F,** Quantitative analyses of **(D)** Col II-positive, **(E)** CD31-positive cells and **(F)** area of marrow cavity based on the results from IHC staining of ectopic bone tissue. (n = 6) **G,** Western blot analysis of protein expression levels of VEGF, OCN and Col I in tissues and cells collected from samples after 14 days of *in vivo* implantation. **H,** Western blot analysis of typical signal pathways associated with osteogenic differentiation (GSK3b, b-catenin, OCN, and Col I) under regulation of an Wnt Antagonist II (IWP-2 inhibitor, 2 μM) for 48h. Asterisk '*' refers to statistical significance when compared to B@M, while Pound '#' refers to the statistical significance when compared to (D+B)@P. **, ##$p < 0.01$. All data were presented as mean ± SD. One-way ANOVA followed by Tukey's post hoc tests was used for comparison.

ability to administer low-dose rhBMP-2 endows this bio-integrated scaffold with substantial potential for clinical large bone regeneration through fully recapitulating the ECO process.

1.6. The spatiotemporally bio-integrated system accelerates the regeneration of segmental radial defects in beagle dogs through enhanced recapitulation of the ECO process

Long bone fracture with low regenerative efficacy remains a very challenging clinical problem. In recent decades, researchers have focused on ECO-based regeneration strategies as much evidence suggests ECO is a more efficient pathway than IMO [63]. Previously, we have dissected the underlying mechanism of the designed spatiotemporally bio-integrated system in each ECO stage and demonstrated its efficiency in rat model with critical-size defects. However, defect sizes in small rodents are unable to mirror the clinical challenges observed in human defects. As a result, larger animals, such as dogs, have been widely used as models for the evaluation of tissue-engineering therapies in large bone regeneration.

In this study, for further unlocking the clinical significance, a large segmental radius defect model in Beagle dogs, the size of which is closer to mankind than that of small rodent animals, was used to investigate and evaluate repair outcomes through the ECO healing route (Fig. 7A). As shown in Micro-CT and X-ray images of Fig. 7B, the defects (visible as translucent areas in X-ray) could still be observed in the B@M group at 12 weeks after the surgery. In contrast the D@M+B@P group demonstrated a notably denser new bone structure, as discerned from the Micro-CT images, when compared to the B@M group. The morphometric analyses further confirmed that the D@M+B@P group exhibited a better of bone healing quality when compared to the B@M. The percentage of BV/TV (Fig. 7C) in the D@M+B@P scaffold group (84.79 ± 5.12 %) was significantly higher than that in the B@M group (64.32 ± 5.52 %) after 12 weeks post-surgery. For BMD (Fig. 7D), the D@M+B@P scaffold group (1.26 ± 0.13 g/cm^3) was significantly higher than B@M group (0.88 ± 0.08 g/cm^3). Sequential fluorescence labelling by injecting varied fluorescent agents at different stages of the healing process is a commonly used technique to assess bone formation rate and new bone integrity. As shown in Fig. 7E and G, the D@M+B@P group demonstrated a significantly higher bone formation rate and improved bone contiguity compared to the B@M group during the advanced stage of ECO healing. To evaluate the morphology of the regenerated tissue, histological analysis and IHC were applied in different time points (Fig. 7H). At week 4 of Safranin O/Fast Green (SO) staining, abundant chondrocytes (SO-positive cells) were observed in both B@M and D@M+B@P (Fig. 7H and I). Although both types of scaffolds could go through repair via the ECO process in the segmental repair model, we observed a higher abundance of chondrocytes and OCN-positive cells in the defect area of the D@M+B@P group compared to the B@P group in the early stage (Fig. 7H–J). Osteoclasts (TRAP-positive cells) were also identified in the constructs from the B@M and D@M+B@P groups, which further facilitated scaffold degradation, BMSC recruitment, and blood vessel invasion (Fig. 7H–K). These results suggest that the D@M+B@P promoted the initial stage of ECO healing through its

hypoxia-mimicking design. After 12 weeks, we found that cortical plates in the D@M+B@P group were nearly fully restored, resulting in successful defect bridging. Van Gieson's (VG) at week 12 (Fig. 7F) provided further evidence by demonstrating the occurrence of loose cancellous bones in the defect regions of the B@M group. In contrast, the D@M+B@P group revealed new, predominantly cortical bones fully supplanting the original defect. This suggests a higher level of skeletal maturity in the D@M+B@P group, pointing to the effectiveness of the spatiotemporally bio-integrated system.

Taken together, these findings demonstrated high practicability and desirable repair outcomes based on the spatiotemporally integrated system when facing defects that were compatible with the actual size of a human. In comparison to the traditional strategy for long bone repair that incorporates single rhBMP-2 and also works through the ECO route, we found that the spatiotemporally integrated system herein could enhance recapitulation of the ECO process and lead to better healing efficiency. These could be ascribed to the hypoxia-mimicking effects in the early stage of ECO, which resulted in high maturity of chondrogenic differentiation and a sufficient degree of hypertrophy. With the aid of follow-up rhBMP-2 release, osteogenic capacity was ultimately improved with promising fracture repair results.

1.7. The spatiotemporally bio-integrated system promotes large maxillofacial regeneration by converting a regular IMO-guided repair to an ECO-dominated repair route

Unlike the long bone fracture, the repair of critical-size bone defects in oral and maxillofacial reconstruction often proceeds through the IMO-guided route [64,65]. In 2002, rhBMP-2 loaded on an absorbable collagen sponge was approved by the FDA and has been widely explored with bone graft materials for bone defect healing since then [66]. However, the efficacy and side effects of BMP-2 for bone regeneration are still major concerns in current clinical orthopedics. As vascularization and osteogenic differentiation are of great importance in IMO-based oral and maxillofacial regeneration, a supraphysiologic dosage of BMP-2 is indispensable that causes non-negligible side effects and cost-effectiveness while providing only incremental benefit. Accordingly, the spatiotemporally bio-integrated system was designed to convert the regular IMO-guided process to ECO-dominated repair route for oral and maxillofacial regeneration. Herein, a critical-size mandible defect in Beagle was used to evaluate this IMO-to-ECO transformation and repair outcomes. Notably, an extremely low-dose rhBMP-2 (around 10 μg) was administrated in this study, while over 200 μg rhBMP-2 was commonly applied in preclinical or clinical trials for the regeneration [66,67]. After 4 weeks of the surgery, the results of Micro-CT reconstructions (Fig. 8A) and X-ray images (Fig. 8B) indicated that only a small amount of bone mineral was deposited within the defects treated B@M group. In contrast, the D@M+B@P group developed a robust cortical shell throughout the fusion bed, which suggested a subtherapeutic dose of rhBMP-2 could induce superior bone healing when combined with DFO-mimicked hypoxia. Furthermore, quantitative assessments showed that the D@M+B@P scaffold group had significantly higher BV/TV percentage than the B@M group, both at 4 and 12 weeks
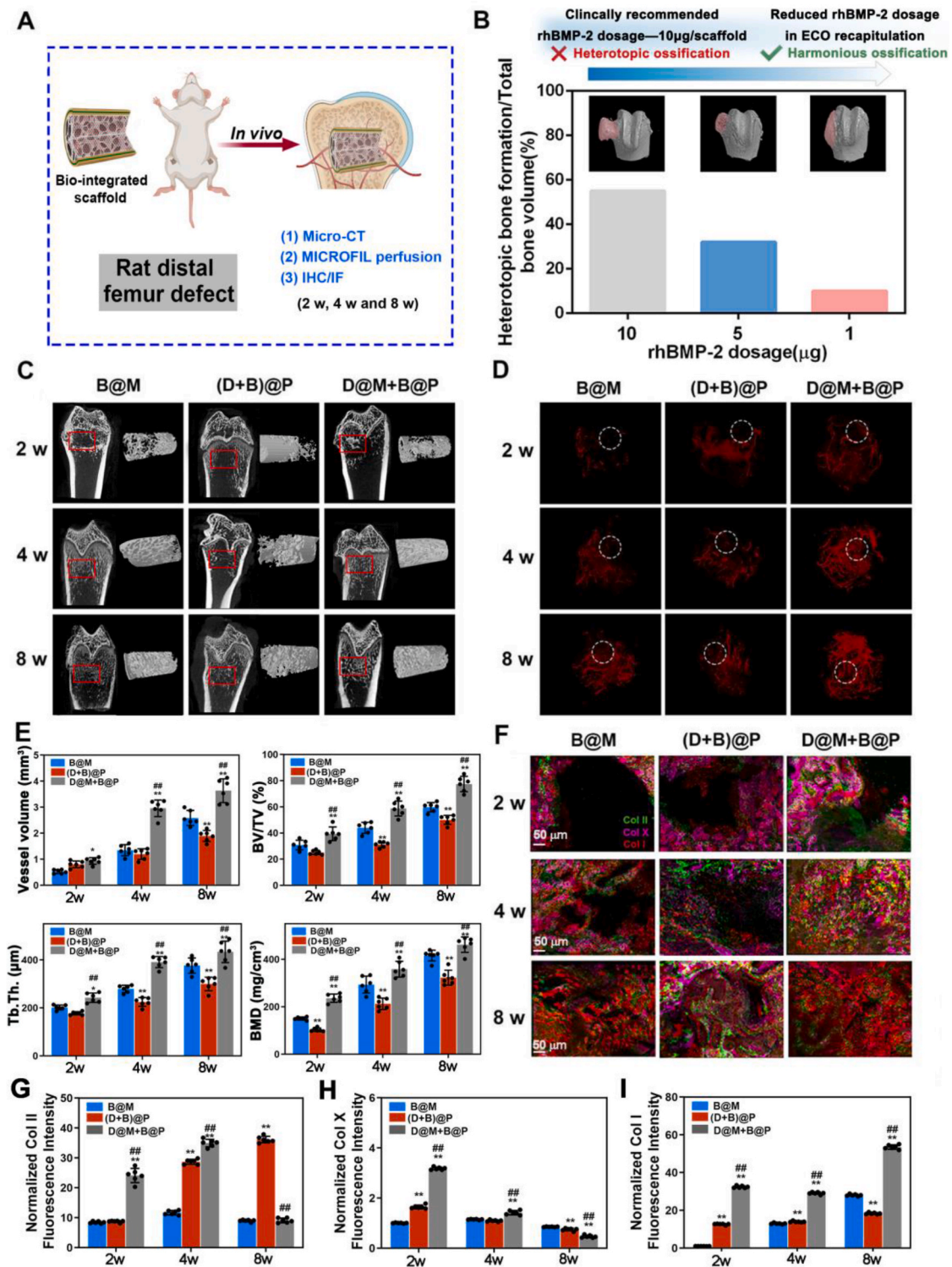
Fig. 6. │ Improved ECO-based regeneration in rat distal femur defect model through spatiotemporally bio-integrated DFO-MBG scaffold with administration of low-dose rhBMP-2. A, Schematics of the experimental design and timeline for illustrating ECO-enhanced regeneration in a rat distal femur defect model facilitated by the bio-integrated scaffolds. **B,** Micro-CT images and quantitative analysis of new bone formation at 4 weeks under varying dosages of rhBMP-2. Administration of high doses of rhBMP-2 (5 μg and 10 μg per scaffold) resulted in significant heterotopic ossification (HO). Red highlighted areas in the representative Micro-CT images indicate the occurrence of HO. **C-D,** Micro-CT and MICROFIL perfusion evaluation of **(C)** new bone formation and **(D)** neoangiogenesis in the reconstruction of femur defects at 2, 4, and 8 weeks. Red and white frames refer to the defect sites. **E,** Statistical analyses of neovascularization and new bone formation at the defect sites. (n = 6) **F,** IHC/IF staining of the central defect region with Col II (green), Col X (pink), and Col I (red) at 2, 4 and 8 weeks. (Scale bar: 50 μm) **G-I.** Quantitative analysis of **(G)** Col II-positive, **(H)** Col X-positive and **(I)** ColI-positive cells from **(F).** (n = 6). Asterisk '*' refers to statistical significance when compared to B@M, while Pound '#' refers to the statistical significance when compared to (D+B)@P. *p < 0.05, **, ##p < 0.01. All data were presented as mean ± SD. Two-way ANOVA followed by Tukey's post hoc tests was used for comparison.
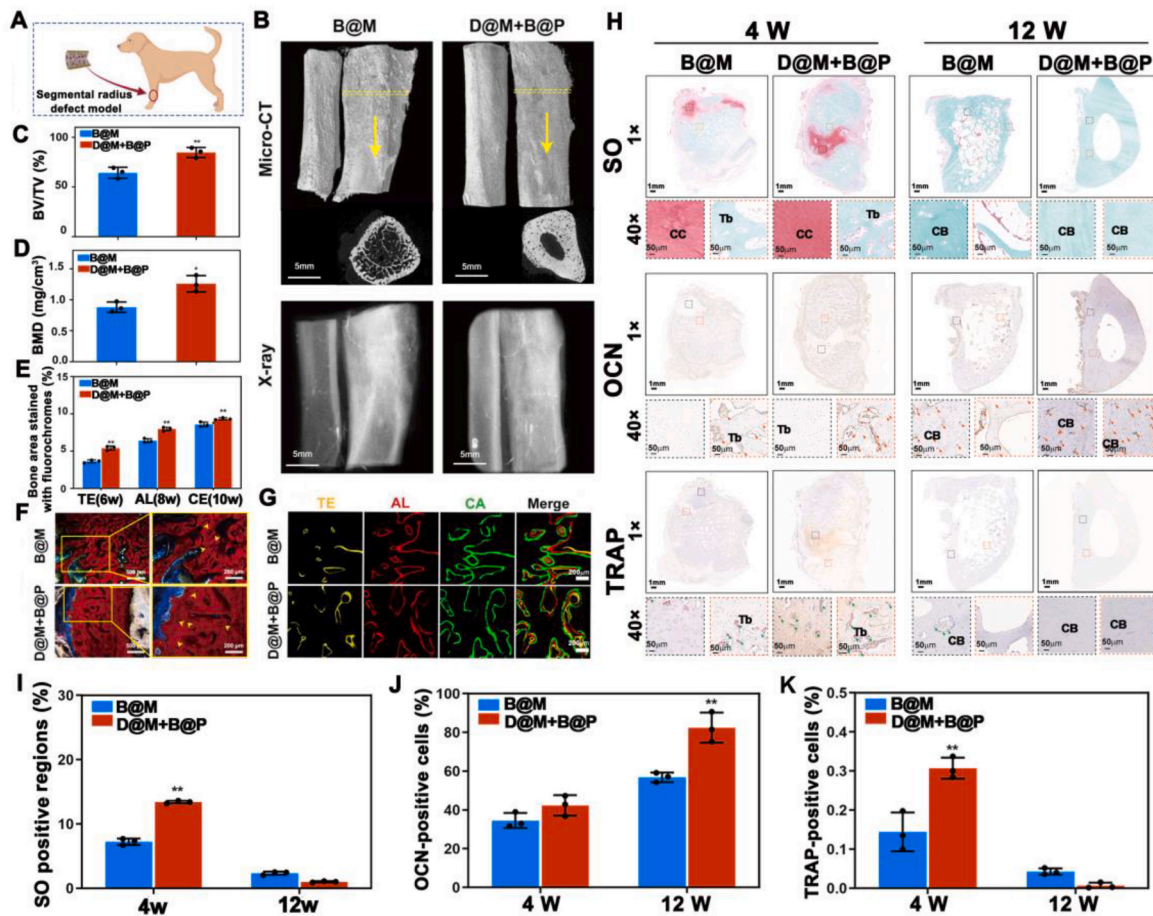
Fig. 7. | The bio-integrated system accelerates the regeneration of segmental radial defects in Beagle dogs through enhanced recapitulation of the ECO process. A, Schematic diagram of segmental radius defect model in Beagle dogs. **B,** Micro-CT analysis and X-ray images at week 12. Yellow dash indicates transverse two-dimensional cross-sectional view along the axis indicated by the yellow arrows. (Scale bar: 5 mm) **C-E,** Statistical analyses of the newly formed bone **(C)** BV/TV and **(D)** BMD in the defect sites newly formed bone in the defect sites from Micro-CT and **(E)** the percentage of fluorochrome area from sequential fluorescence labelling displayed in **(G)**. (n = 3). The percentage of BV/TV in the D@M+B@P scaffold group (84.79 ± 5.12 %) was significantly higher than that in the B@M group (64.32 ± 5.52 %) at 12 weeks after surgery. For BMD, the D@M+B@P scaffold group (1.26 ± 0.13 g/cm^3) was significantly higher than B@M group (0.88 ± 0.08 g/cm^3). **F,** VG staining of undecalcified sections at week 12. Yellow arrows indicate blood vessels. (Scale bar: 500 μm and 200 μm for low and high magnification, respectively) **G,** Sequential fluorescence labelling of tetracycline (TE, yellow), alizarin red (AL, red) and calcein (CA, green) during week 8–12. (Scale bar: 200 μm) The D@M+B@P group showed a significantly higher bone formation rate and improved bone contiguity compared to these of the B@M group. **H,** Safranin O/Fast green (SO) and immunohistochemical (IHC) evaluation for extracellular matrix components present in defects. CC: Chondrocytes, Tb: Trabecula bone, CB: Cortical bone. (Scale bar: 1 mm and 50 μm for low-power (1 ×) objective in SO staining and high-power (40 ×) objective in SO staining and immunohistochemical staining (OCN and TRAP), respectively) **I–K,** Quantitative analyses of **(I)** SO positive regions, **(J)** OCN-positive cells and **(K)** TRAP-positive cells based on the results from IHC staining (n = 3, three slice replicates in each cohort). *p < 0.05, **p < 0.01, All data were presented as mean ± SD. Two-tailed Student's t-test or two-way ANOVA followed by Tukey's post hoc tests was used for comparison.

post-surgery (Fig. 8C). Histological analysis provided further validation of these findings (Fig. 8D–G). Due to the IMO-dominated repair pathway, only fibrous tissue, not cartilage, was observed in the medullary cavity in the B@M group at 4 weeks. BMP-2 alone can induce abundant recruitment of proliferative cells around the defect, forming fibrous connective tissue. However, new bone formation relies on the invasion of functional blood vessels, which was found limited in B@M group. By contrast, the bio-integrated system displayed notable chondrocytes and significant higher SO positive regions at 4 weeks (Fig. 8D–E), with no remaining scaffold detectable in the mandible defect. This suggests that the defect sites had been replaced by cartilage intermediate and regeneration followed an ECO-dominated process. Osteoblasts and osteoclasts were also quantified (Fig. 8F–G), and the D@M+B@P group exhibited a higher presence of TRAP-positive cells (osteoclasts) in comparison to the B@P group, indicating an accelerated degradation of the D@M+B@P scaffold matrix and thus contribute to cartilage formation and ECO-healing process. After 12 weeks, the B@M group displayed less effective repair results, characterized by a thin

cortical shell around the cavity. On the other hand, the D@M+B@P group exhibited a fully formed compact bone structure. Moreover, a higher number of OCN-positive cells (osteoblasts) were observed in the D@M+B@P group compared to the B@P group, indicating superior regenerative outcomes. These observations are consistent with Micro-CT and X-ray findings, which demonstrate that the D@M+B@P group facilitates repair via an ECO-dominated healing route, thus enhancing the overall bone regeneration outcomes.

Herein, the transformation of the repair pathway from IMO-guided route to ECO-dominated route was successfully obtained through the spatiotemporally bio-integrated system. According to our knowledge, this is the first strategy to involve a tissue engineering design to realize such healing route shift for improved regenerative outcomes. Multiple studies have evidenced that Hh signaling and related receptor (e.g., Smoothened (Smo)) are able to direct the ossification routes [68]. Without Ihh or Hh receptor Smo, osteoblasts cannot form during the ECO process [69,70]. Previously, by applying HIF-1α signaling pathway inhibitor, we have found HIF-1α was the key factor to enhance Ihh and
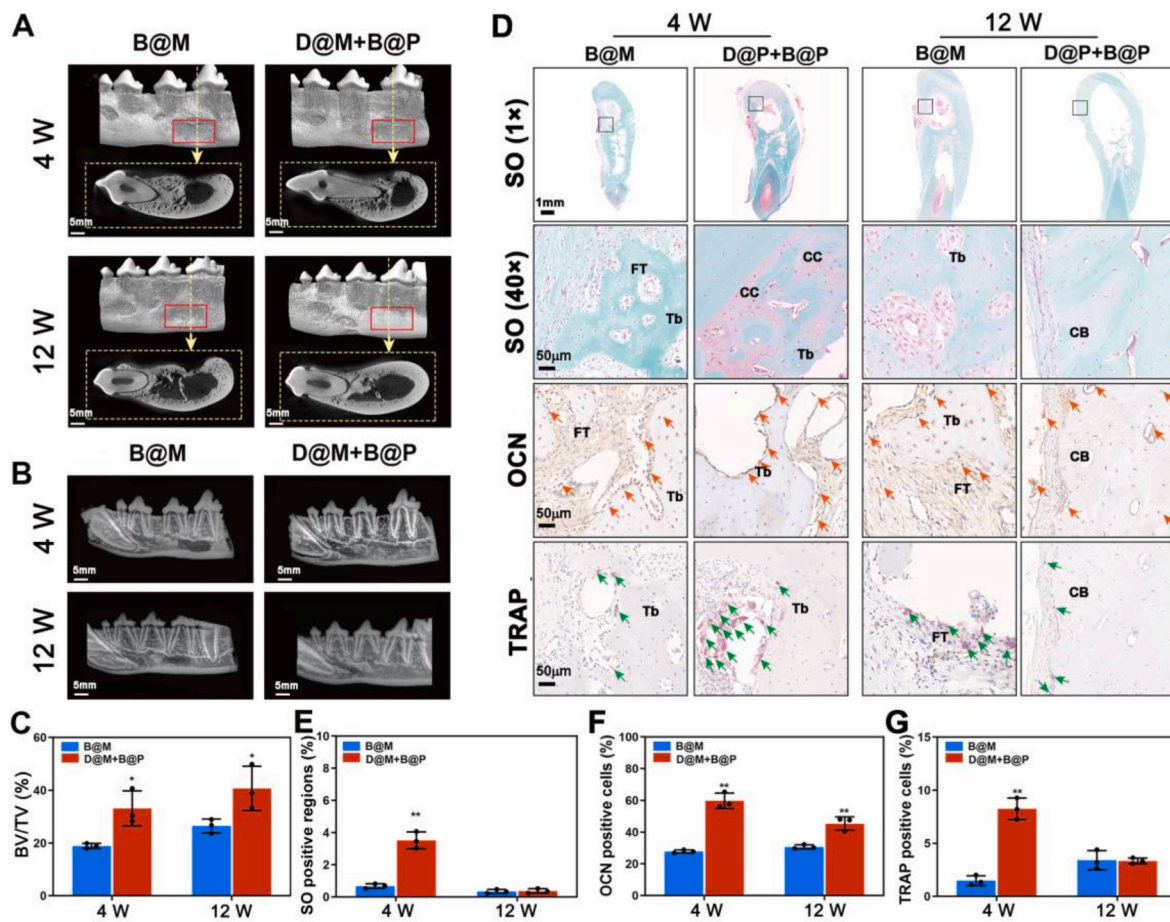
Fig. 8. | The bio-integrated system promotes large mandible defect regeneration through an ECO-dominated pathway rather than IMO-guided route. **A**, Micro-CT analysis at week 4 and 12. The solid red box indicates defect sites, while the yellow dotted box illustrates sagittal two-dimensional cross-sectional view along the axis indicated by the yellow arrows. (Scale bar: 5 mm) **B**, X-ray images at week 4 and 12. (Scale bar: 5 mm) **C**, Statistical analysis of the newly formed bone (BV/TV) in the defect sites (n = 3). From the quantitative assay, the percentage of BV/TV in the D@M+B@P scaffold group (40.69 ± 8.39 %) was significantly higher than that in the B@M group (26.47 ± 2.66 %) at 12 weeks post-surgery. **D**, Safranin-O/Fast green (SO) staining and immunohistochemical (IHC) staining (OCN and TRAP) on tissue sections from two groups after 4 and 12 weeks. Red arrows indicate OCN-positive cells, while green arrows indicate TRAP-positive cells. CC: Chondrocyte, Tb: Trabecula bone, CB: Cortical bone, FT: Fibrous tissue. (Scale bar: 1 mm and 50 μm for low-power ($1 \times$) objective in SO staining and high-power ($40 \times$) objective in SO staining and immunohistochemical staining (OCN and TRAP), respectively) **E-G**, Quantitative analyses of **(E)** SO positive regions, **(F)** OCN-positive cells and **(G)** TRAP-positive cells through using immunohistochemical staining (n = 3, three slice replicates in each cohort). *$p < 0.05$, **$p < 0.01$, All data were presented as mean $\pm$ SD. Two-way ANOVA followed by Tukey's post hoc tests was used for comparison.

Wnt signaling pathways for early chondrogenic differentiation and maturation. That is, HIF-1α induced by the DFO-mimicked hypoxia in the bio-integrated system contributes throughout the healing process and is the driving force to convert IMO-tended repair to ECO-based regeneration, thereby improving regenerative efficiency with low-dose BMP-2.

1.8. Clinical perspectives

Despite the great prospects ECO recapitulation has shown during the bone healing process, challenges and obstacles remain before its wide applications for large bone regeneration in the clinical. Currently, the primary difficulties are prolonged *in vitro* culture and the complexity of growth factors accompanied by high treatment costs and adverse effects. These issues render ECO-based approaches unavailable for clinical translation and commercialization. Therefore, a novel ECO-dominated strategy based on a hypoxia-mimick scaffold with low-dosage BMP-2 administration herein is very promising and is supposed to pave a clear path to success in clinical use (Scheme 2). In the system, DFO-anchored MBG porous scaffold is demonstrated to effectively initiate hypoxia microenvironment and thus enhance the cartilage induction process, while the sustained release of low-dose BMP-2 existed in the later stage

can induce sufficient ossification. Notably, DFO, as an iron chelator that has been widely used in treating iron overload, together with a potent bone-induction growth factor BMP-2, have been both approved by FDA with strong and adequate clinical evidence. That is, the combination of these two in one system has strong clinical benefits with huge potential for future clinical endorsement and applications. Accordingly, DFO-anchored MBG can significantly improve safety and cost-effectiveness while low dosage of BMP-2 controllable release, which reduces the side effect and is of great significance in clinical application.

The enhanced and precisely regulated ECO process was proved to show sound repair effects in both regular rodent animals and large animal models. Unlike most preclinical studies that simply use small rodent animals with relatively low critical dimension of defects, this integrated DFO/BMP-2 system demonstrated augmented large bone regeneration through ECO-dominated route in Beagles with two different critical-size defect models. Most importantly, harmonious regeneration can be achieved not merely in the ECO-tended large segment defect of the long bone but also in the intramembrane osteogenic microenvironment, where IMO-tended healing could be converted to the more efficient ECO repair route. Moreover, even under low-dose BMP-2, there are desired repair outcomes in all types of defect models, which are of great significance for clinical translation and wide
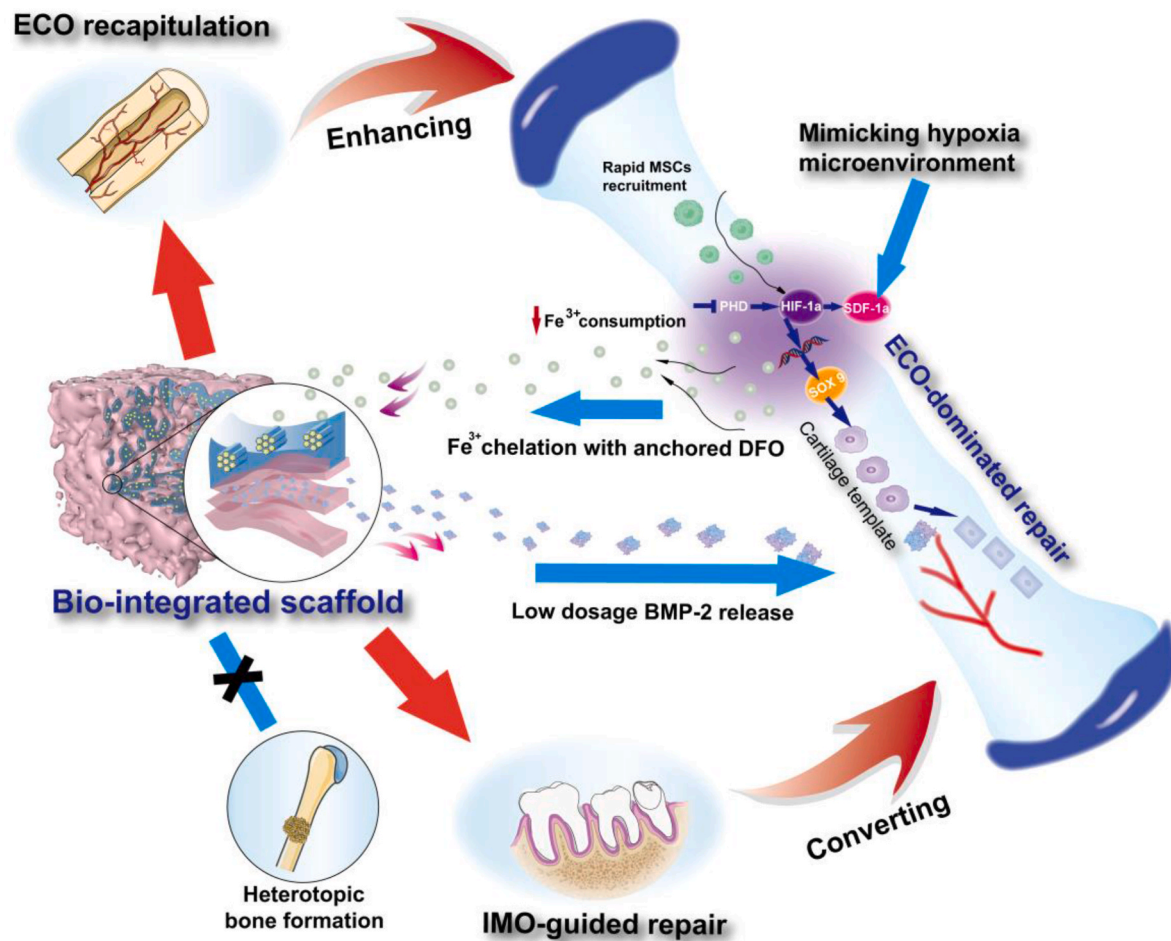
Scheme. 2. | Schematics of the bio-integrated system designed for enhancing large bone regeneration via an ECO-dominated route. This strategy employed a well-orchestrated combination of biomimetic hypoxia induced by DFO and administration of low-dose rhBMP-2. Specifically, DFO chemically anchored within the mesopores of MBG scaffold mitigated the toxicity of free chemicals and effectively mimics the hypoxic microenvironment. Through assembly of PEGS layers, DFO and rhBMP-2 were delicately segregated for maximum bioactivity. Moreover, this bio-integrated system facilitated the precise programming of low-dose rhBMP-2 release, which can minimize the side effects associated with rhBMP-2, such as heterotopic bone formation. In a variety of defect models, such as the rat femur defect and the dog segmental defect, the bio-integrated system exhibited an enhanced recapitulation of ECO, thereby facilitating high-quality large bone regeneration. Notably, in the dog mandibular defect model with clinically relevant size, which typically heals primarily via the IMO route, this bio-integrated system effectively converted the healing process from an IMO-guided pathway to the more efficient ECO-dominated repair route, resulting in superior reconstruction. Accordingly, we believe these encouraging findings demonstrate substantial potential of this bio-integrated design for enhancing large bone repair via an ECO-dominated route and addressing significant clinical challenges.

application. We believe the developed bio-integrated system with potent hypoxia-mimick initiation and optimized BMP-2 administration is a promising approach through ECO-dominated healing route for large bone regeneration in future clinical use.

2. Materials and methods

2.1. Materials and animals

3-Aminopropyltrimethoxysilane (APTMS) and glutaraldehyde were purchased from Aladdin (USA). Desferoxamine (DFO) and dibenzocyclooctyne-amine (DBCO-NH$_2$) were purchased from Sigma (USA). PEG (Mw = 600 g/mol), succinic anhydride, N, N′-diisopropylcarbodiimide (DIC) and N-hydroxy succinimide (NHS) were purchased from Aladdin (USA). 3-azido-1-propylamine (Az-NH$_2$) was purchased from TCI (USA). Recombinant human BMP-2 was obtained from Shanghai Rebone Biomaterials Co. Ltd. (Shanghai, China). Tetraethyl orthosilicate (TEOS), Ca (NO$_3$)$_2$·4H$_2$O and triethyl phosphate (TEP) were obtained from Shanghai Ling Feng Chemical Reagent Co., Ltd. (Shanghai, China). A human BMP-2 ELISA kit, tetracycline

hydrochloride and Pluronic®F-127 (EO$_{106}$PO$_{70}$EO$_{106}$) were purchased from Sigma–Aldrich (USA).

All experimental animals were obtained from Shanghai Jiao Tong University School of Agriculture and Biology. The animal experiments were performed in strict accordance with the NIH Guide for the Care and Use of Laboratory Animals, and all procedures were carried out by the Animal Research Committee of Sixth People's Hospital, Shanghai Jiao Tong University School of Medicine (License number: SCXK (Hu) 2017-0007, SYXK (Hu) 2018-0006; Animal research ethics number: NO. DWLL20220602)

2.2. Preparation of hypoxia-mimicking scaffolds (MBG-DFO)

MBG based scaffold was prepared by a modified sol-gel and polyurethane (PU) foam templating process as reported before [28]. Briefly, the preparation process involved dissolving 4 g of F127, 1 g of HCl (0.5 M), 0.76 g of Ca(NO$_3$)$_2$·4H$_2$O, 0.23 g of TEP, and 5.20 g of TEOS in 50 mL of ethanol. This mixture was then stirred at 40 °C for 24 h to form the MBG sol. Subsequently, the sol was subjected to rotary evaporation at 60 °C for 30 min, resulting in an MBG sol with optimal viscosity.

Following this, 6 g of the viscous sol was thoroughly blended with 2 g of polyacrylic acid microspheres (serving as the microporous template), which was then uniformly impregnated into a PU sponge. The samples underwent a drying process at 60 °C for 72 h, followed by a heat treatment regimen at 600 °C for 5 h to eliminate all organic templates, including PU foam, F127, and polymer microspheres. This process resulted in the production of MBG scaffolds.

For functionalization of MBG scaffolds, there included three steps. First, the MBG scaffolds were functionalized with amino acids. Briefly, MBG (200 mg) was dried and immersed in anhydrous toluene (100 mL), and then APTMS was added and refluxed at 80 °C for 24 h. The scaffold was removed and washed with toluene and absolute ethanol three times before vacuum drying. Second, MBG-NH₂ scaffolds (200 mg) were immersed in 100 mL of ultrapure water, and 4 mL of glutaraldehyde was added. The solution was stirred at 37 °C for 6 h, followed by washing and drying. This intermediate product was termed as MBG-CHO. Finally, the MBG-CHO scaffolds (200 mg) were reacted with DFO (100 mg) in 100 mL ultrapure water at 37 °C for 6 h. After washing and drying, the MBG scaffolds were functionalized with DFO.

2.3. Preparation of PEGS hydrogel by click chemistry

First, we synthesized functionalizable PEGS prepolymers according to previously published methods (Fig. 2A) [37]. Briefly, linear PEGS-OH prepolymers was synthesized via epoxide ring-opening polymerization of diglycidyl sebacate (DGSE) (1 eq), bis(tetrabutylammonium) PEG carboxylate (TBAP) (1 eq) and a catalyst (Bis(tetrabutylammonium) sebacate (TBAS) at 0.6 mol%. These monomers and catalyst were dissolved in anhydrous dimethylformamide (DMF) and transfer to a glove box within a Schlenk flask filled with high purity nitrogen. After sealing, the flask was removed from the glove box and connected to a Schlenk line, followed by heating at 100 °C. Finally, the PEGS-OH product was precipitated in ethyl ether and dried overnight at room temperature under vacuum.

For further carboxy-modification of PEGS prepolymers (PEGS-COOH), the prepared linear PEGS-OH prepolymers (1 eq) and succinic anhydride (99 %, Aladdin) (2 eq) were dissolved in anhydrous DMF and then stirred at 100 °C under nitrogen atmosphere for 1 h before being concentrated. Then, 1 mL mixture of DIC (99.5 %, Aladdin) (0.5 mmol) and NHS (98 %, Aladdin) (0.5 mmol) in anhydrous dimethyl sulfoxide (DMSO) was then added dropwise into the PEGS-COOH solution under nitrogen atmosphere. After overnight reaction, the mixture was dialysed and lyophilized to remove impurities. For preparing PEGS hydrogel with various crosslinking degrees (60 %, 80 % and 100 %), the grafting ratios of Az-NH₂ and DBCO-NH₂ were mediated by varied feeding ratios of monomers in PEGS hydrogel (molar ratios (-COOH: NH₂): 1:0.6, 1:0.8 and 1:1). As for assembling PEGS hydrogel on the scaffolds, PBS solutions of PEGS-Az (30 % wt) and PEGS-DBCO (30 % wt) were loaded in syringe. Upon the injection, a PEGS layer was formed within 5 min at room temperature.

2.4. Simulation of fluid flow and mass transfer in MBG scaffolds

3D MBG model was constructed as previous study using SIMULIA Abaqus software (Version 2020, Dassault Systèmes, FRA) with the porosity set as 70 % [71]. The model was then imported into Simcenter STAR-CCM+ (Siemens Digital Industries Software, DE) for meshing and calculation. After meshing, the scaffold was surrounded by four boundary sides, an inlet, and an outlet. To check the mass transfer capacity in different MBG scaffolds, the inlet velocity against outlet direction was defined as 1.0 mm/s, which is in the normal range of capillary blood flow rate. The pressure values on the wall surface of the scaffold struts were calculated and illustrated through the plane across the flow direction. The detailed information of simulated model was included in supplemental materials.

2.5. FT-IR and ¹HMNR characterization

The chemical structure of the scaffolds and PEGS derivatives was characterized by Fourier transform infrared (FT-IR) spectroscopy (Nicolet 6700, Thermo Fisher) recorded in the range of 500–4000 cm⁻¹. The structures of PEGS derivatives were also characterized by nuclear magnetic resonance (NMR) spectroscopy (Bruker AVANCE III 600, Bruker Corporation). The data were presented and analyzed using MestReNova NMR software.

2.6. EDS and ICP assays

The iron chelation ability of the MBG-DFO scaffold was performed. The prepared MBG-DFO scaffold was immersed in a 3 mM ferric chloride (FeCl₃, Sigma) solution. After 1 h, the scaffold was removed and washed with ultrapure water, followed by drying. The iron in the scaffolds was imaged by energy-dispersive X-ray spectroscopy (EDS). To evaluate the Fe ion adsorption kinetics, the adsorption curves were acquired, and the amounts of adsorbed Fe were presented as qt (mg/g), which were calculated according to Eq (1):

$$qt = \frac{(ci - ct)v}{m}, \tag{1}$$

where ci and ct (mg/L) are the initial and the remaining Fe concentrations at sampling at time t, respectively; v(L) is the volume of the Fe solution; and m (g) is the initial mass of the scaffolds.

2.7. Far-ultraviolet circular dichroism spectra

Far-ultraviolet circular dichroism spectra (CD) made on a spectropolarimeter (Model J-715, Tokyo, Japan) with a 0.1 cm path length rectangular quartz cell was used to measure the absorption difference between left-handed and right-handed circularly polarized light of rhBMP-2 protein, and then to analyze the conformational changes of rhBMP-2. CD spectra were taken in a wavelength range of 190–260 nm and the content of the secondary structure of proteins was calculated using CDNN Deconvolution software (version 2.1; Bioinformatik.biochemtech.uni-halle.de/cdnn).

2.8. Degradation profiles of PEGS hydrogels

To test the degradation properties of PEGS hydrogels with different degrees of crosslinking, 20 mg PEGS hydrogel was dissolved in 5 mL PBS solution (pH = 7.2). The PBS containing degradation products was refreshed with new PBS every two days. The duration for the complete degradation of the hydrogels was recorded.

2.9. Spatiotemporal immobilization of DFO and rhBMP-2

According to whether DFO or rhBMP-2 was present, there were five groups of scaffolds, which were referred to as MBG, B@M, D@M, (B+D)@P and D@M+B@P. rhBMP-2 was entrapped in the PEGS hydrogel to prepare rhBMP-2-loaded MBG (B@M) and separated from the MBG substrate by a PEGS layer to achieve the spatiotemporal integration of rhBMP-2 and DFO (D@M+B@P). Direct combination of rhBMP-2 and DFO was introduced to prepare the (D+B)@P scaffold. The outer surface of the scaffolds was another PEGS coating. The PEGS hydrogel endowed rhBMP-2 with the properties of spatiotemporal distribution and sustained release. Briefly, rhBMP-2 solution (saturated scaffold-holding volume) containing different contents of rhBMP-2 was added to the MBG-based scaffold and incubated for 4 h for complete adsorption. The detailed information of rhBMP-2/DFO-MBG scaffolds used in this manuscript was listed in Table 1 with schematics shown in Fig. S1. For experiments in mice and rats, MBG scaffolds with a size φ of 2.5 mm × 5 mm were prepared. For regeneration of rat femur defects, a 10 μg

high dose and a 1 μg low dose of BMP-2 were applied. For reconstruction of truncated radial defects in the beagle dog model, MBG scaffolds with a size φ of 7 mm × 20 mm were prepared, and a 20 μg low dose of BMP-2 was applied. For reconstruction of mandibular defect defects in beagle dogs, MBG scaffolds with a size of 10 mm × 5 mm × 5 mm and a low dose of BMP-2 (10 μg) were applied. Detailed parameters are shown in Table 2.

2.10. Scanning electron microscopy (SEM) and transmission electron microscopy (TEM)

The micromorphology of the MBG-based scaffold was observed using field emission scanning electron microscopy (SEM; Hitachi S-4800). The mesoporous structure of the scaffolds was examined using transmission electron microscopy (TEM, JEM-2010, Japan).

2.11. Release profiles of rhBMP-2

Before investigating release profiles of B@M and D@M+B@P scaffolds, the two kind of scaffolds (Φ2.5 mm × 5 mm) containing 1 μg of rhBMP-2 were made. For B@M, 1 μg of rhBMP-2 in 5 μl PEGS solution was dripped onto the MBG scaffold. For D@M+B@P scaffold, 2.5ul PEGS layer, 5 μl PEGS layer containing 1 μg of rhBMP-2 and 2.5 μl PEGS layer were coated sequentially onto the MBG-DFO scaffold. The scaffolds were vacuum-freeze-dried overnight. *In vitro* release curves for the B@M and D@M+B@P groups were obtained. Briefly, scaffolds were immersed in PBS and shaken at 37 °C. At each time point, the soaking solution was completely collected, and the same volume of PBS was added. The content of released rhBMP-2 was calculated by using a human BMP-2 ELISA kit.

2.12. Isolation and culture of rBMSCs

Rat bone marrow stromal cells (rBMSCs) were harvested from rat bone marrow. Four-week-old male SD rats were sacrificed and immersed in 75 % alcohol for 10min. Then femur and tibia were taken out, and bone marrow was flushed out with a-MEM supplemented with 10 % FBS and 1 % antibiotics (100 U mL^{-1} penicillin G and 100 μg mL^{-1} streptomycin sulphate). The bone marrow suspension was put in tissue culture polystyrene flask and incubated at 37 °C in a humidified atmosphere containing 5 % CO_2. The extracted rBMSCs were recorded as passage 0. Passage 2–5 of rBMSCs were used in this study and were verified with rBMSCs markers by flow cytometry.

2.13. Western blot and immunofluorescence staining

To examine the influence of bio-integrated scaffolds on the expression of HIF-1α and proteins related to cell recruitment, rBMSCs (2 × 10^4 cells/well) were seeded on 24-well plates where the B@M, (D+B) @P and D@M+B@P scaffolds were in the Transwell® chamber. After 24 h, rBMSCs were washed with PBS and extracted with RIPA lysis solution containing 1 mM phenylmethanesulfonyl fluoride (PMSF) to prevent proteolysis. To investigate the effect of scaffolds on the expression of chondrogenesis and osteogenesis, the related proteins was extracted from tissues in tissues and cells from the samples after 3-day *in vivo* implantation. For Western blot analysis exploring specific signal pathways associated with chondrogenic differentiation, rBMSCs (2 × 10^4 cells/well) co-cultured with the B@M, (D+B) @P and D@M+B@P scaffolds were pre-treated with or without HIF-1α inhibitor (LW6, 20 μM, Sigma-Aldrich) for 24 h and then cultured without the inhibitor for another 2 days. Similarly, for the Western blot analysis focused on the signal pathways associated with osteogenic differentiation, rBMSCs (2 × 10^4 cells/well) were co-cultured with the B@M, (D+B) @P and D@M+B@P scaffolds for 3 days and then treated with or without IWP-2 inhibitor (2 μM, Sigma-Aldrich) for 48 h. All these extracted proteins were analyzed using a BCA kit and separated by 10 % SDS–PAGE. The

separated protein samples were transferred to polyvinylidene difluoride membranes. The samples were incubated with primary antibodies, HRP-conjugated secondary antibody (Abcam, Cambridge) and ECL plus reagents (Tanon, Shanghai) for exposure. The original images of Western blot band were shown in Fig. S8.

For fluorescence staining, cells cultured for 24 h were fixed with 2.5 % glutaraldehyde for 10 min and blocked with 10 % goat serum for 1 h. Then, the cells were incubated with HIF-1α primary antibody (abcam, ab179483) at 4 °C overnight and Alexa Fluor 647-labelled goat anti-rabbit secondary antibody (Abcam, Cambridge) for 2 h at 37 °C. FITC-phalloidin (Sigma, St Louis, USA) was applied to observe the cytoskeleton, and DAPI (Sigma, St Louis, USA) was applied to stain nuclei. The expression of HIF-1a and cell morphology were observed by using confocal laser-scanning microscopy (CLSM, A1, Nikon). *In vivo* rBMSC recruitment was evaluated by staining. Scaffold samples implanted in rat distal femur defect for 3 days were removed and fixed with 4 % PFA. Then, the samples were decalcified, dehydrated and embedded for sectioning (4.5 μm). The sections were deparaffined, stained with BMCS-related antibodies (CD44 (abcam, ab238464), CD90 (ab92574)) and observed by confocal laser-scanning microscopy [72].

2.14. Migration assay

In vitro cell migration was evaluated by Transwell® assays. The scaffolds implanted in rat distal femur defects for 3 days were removed and placed in a 24-well plate. rBMSCs (1 × 10^4) were seeded in Transwell® chambers and cultured for 24 h. The upper face of the chamber was cleaned with a cotton swab. Then, the chamber was fixed with 4 % PFA and stained with 1 % crystal violet stain solution. After washing with PBS three times, the chamber was placed onto a coverslip and observed by inverted microscopy. The number of migrating cells was calculated using ImageJ.

2.15. Quantitative PCR

For the RT–PCR experiment, total RNA from the constructs was isolated with TRIzol (Takara, Tokyo, Japan) and converted into complementary DNA (cDNA) using the PrimeScript RT reagent kit (Takara, Tokyo, Japan). The cDNA was amplified by an RT–PCR system containing SYBR Premix Ex TaqTM and primers (for typical hypoxia, chondrogenic, osteogenic and vascular genes) using a Bio-Rad CXF96 PCR system (Bio-Rad Laboratories, USA). The hypoxia genes included HIF-1α and PHD2. The chondrogenic differentiation genes include Col II, Sox 9 and Acan. The osteogenic differentiation genes included TGF-β1, BMPR1A, BMPR1B, BMP2, RUNX2, OPN, OCN, and Col I. The vascular genes included VEGF, SCF, and PLGF. Primer sequences used in this study were listed in Table S2.

2.16. mRNA-seq analysis

The samples were removed 3 days after implantation and immediately placed into TRIzol for mRNA-seq analysis. Total RNA from tissues was extracted by using TRIzol reagent according to the manufacturer's instructions. After extraction and sedimentation with chloroform and isopropyl alcohol, the RNA pellet was washed twice with 1 mL 75 % ethanol and air dried for 10 min. Then, RNA was dissolved with the addition of DEPC-treated water. Total extracted RNA, quantified with a NanoDrop and Agilent 2100 bioanalyzer (Thermo Fisher Scientific, MA, USA), was then purified with Oligo(dT)-attached magnetic beads. The product was evaluated on an Agilent Technologies 2100 bioanalyzer for quality control. The final library was established with phi29 to make DNA nanoballs (DNBs) containing 300 copies of one molecule. After that, the DNBs were loaded into the patterned nanoarray, and single-end 50-base reads were performed on the BGIseq500 platform (BGI-Shenzhen, China). DEGs identified in groups was shown in Tables S3–S5.

2.17. In vivo mouse ectopic bone model

The model of ectopic bone formation in thigh muscle pouches of mice was used to evaluate the hypoxia-mimicking and osteogenesis process *in vivo*. For ectopic bone formation, 5 μg rhBMP-2 was applied to each scaffold. C57BL/6 male mice aged 8–10 weeks were from Shanghai Jiao Tong University School of Agriculture and Biology. The details were shown in supplemental methods.

2.18. In vivo rat distal femur defect model

Eight-week-old male SD rats were used as an *in-situ* model. Femur defects were made on both sides (2.5 mm diameter × 5 mm length) and washed with normal saline to remove tissue residue. Then, different scaffolds (B@M, (D+B) @P, D@M+B@P) were implanted in the defect. At a specific time, the rats were sacrificed, and femurs with defects were removed. After fixing with 4 % PFD, the samples were used for micro-CT and MICROFIL perfusion tests. Then, the samples were subjected to sectioning and stained with primary antibodies against Col I, Col II, and Col X. The antibody information used in this study could be found in Table S1.

2.19. In vivo dog mandibular critical-sized defect and dog segmental radial defect models

To successfully translate this approach from proof-of-concept rodent studies to clinical reality, safety and efficacy must first be evaluated in large animal models such as sheep, goats, pigs, or dogs [73]. The dog represents an excellent translational model. Compared with rodents, dogs have more genetic diversity. At the same time, dogs can more easily undergo treatment. Importantly, dogs are more suitable for preclinical evaluation before conversion to human use [74]. Twenty-four healthy adult male beagle dogs (12 months old and weighing 11–13 kg) were used for preclinical evaluation. All procedures were approved by the Institutional Animal Care and Use Committee of Shanghai Jiao Tong University.

For reconstruction of mandibular critical-sized defects, twelve beagles were randomly divided into two groups (B@M and D@M+B@P) and two time points (4 w and 12 w). For the basic anesthesia of dog, "Zoletil® 50" was used for intramuscular injection as 0.08 mL/kg. For respiratory anesthesia, isoflurane was used for surgical procedure. Xylazine Hydrochloride Injection (intramuscular injection as 0.01 mL/kg) was used for anesthesia. After anesthesia, the beagle was placed in the lateral position, and the surgical site was disinfected. The mandibular region of the right premolars was exposed, and the outer layer of bone (10 × 5 × 5 mm^3) was cut off. Then, the cuboid scaffold was tightly implanted into the defect. At 4 and 12 weeks after the operation, the beagles were euthanized, and the mandible specimens were removed.

For reconstruction of critical-size segmental radial defects, twelve beagles were randomly divided into two groups, B@M and D@M+B@P and two time points (4 w and 12 w). After anesthesia, the skin was cut open, and the left radius of the beagle dog was exposed (Fig. S11). At the same time, a critically sized segment of the shaft (20 mm) was cut off to create a segmental fracture [75]. Then, a cylindrical scaffold was implanted into the bone defect gap. At week 4 and 12, the beagles were euthanized, and the radius was removed.

2.20. Micro-CT analysis and magnetic resonance imaging (MRI)

For microcomputed tomography (Micro-CT), the samples were fixed in 4 % paraformaldehyde for 3 days, and measurements were carried out at beamline BL13W of the Shanghai Synchrotron Radiation Facility (SSRF, Shanghai, China). All bone samples were scanned, and 2D slices were obtained. Then, 3D reconstruction was performed with VG Studio MAX software (Volume Graphics, Germany). The quantitative analysis of the region of interest (ROI) was performed with the relative new bone volume fraction (BV/TV) and trabecular bone thickness (Tb.Th). In the Micro-CT analysis of distal femur defect model in rats, the lower grey threshold was set as 68 while the upper grey threshold was set as 255, with a total volume-of-interest (VOI) of 42.55565 mm^3. For dog mandibular large defect model, the lower grey threshold was set as 80 while the upper grey threshold was set as 255, with a total VOI volume set as 362.45976 mm^3. For dog segmental radial defect model, the lower grey threshold was set as 90 while upper grey threshold was set as 255, with a total VOI volume of 839.51144 mm^3. As for phantom calibrations, water was used as reference and the Hounsfield units (HU) was set as "22.91432". The samples underwent magnetic resonance imaging (MRI) performed on a 3.0 T scanner (Ingenia, Philips Healthcare, Best, Netherlands) at 4 and 12 weeks after surgery.

2.21. MICROFIL perfusion

To observe and evaluate blood vessel formation, MICROFIL perfusion (MICROFIL, MV-122) was applied. After anesthesia with sodium pentobarbital, the chest chamber was opened, followed by ligation of the bilateral pulmonary trunks and descending aorta. The ventricle was punctured with an indwelling needle and vascular catheter and perfused with heparin solution. Then, 20 mL of MICROFIL in each rat was perfused. After perfusion, the rats were placed at 4 °C overnight to solidify the filling liquid. Femur samples were collected, fixed, and decalcified for micro-CT.

2.22. Sequential fluorescent labelling and Van Gieson's staining

Sequential fluorescence labelling was applied to evaluate the new bone. Beagle dogs were injected with 25 mg/kg tetracycline (TE), 30 mg/kg alizarin red (AR) and 20 mg/kg calcein (CA) at 6, 8 and 10 weeks, respectively. At week 12, the dogs were euthanized, and radius samples were obtained. The obtained samples were then embedded in PMMA and sliced into sections approximately 150 μm thick using a hard tissue microtome. Then, the slices were polished, and the final thickness was approximately 40 μm (transverse slice direction of the central portion within the segmental radial defect area). The sections were evaluated by CLSM to observe the fluorescence labelling of these undecalcified bone tissues. Undecalcified samples were stained with van Gieson's picro fuchsin (VG) [10] and observed a light microscope (Nikon E100, Japan).

2.23. Histology and immunohistochemistry

The samples were fixed with 4 % PFD, decalcified 15 % EDTA solution, dehydrated and embedded in paraffin for sectioning (4.5 μm). The sections (transverse slice direction of the central portion within the segmental radial defect area; sagittal slice direction of the central part within the mandibular defect area) were stained with safranin O/Fast Green for the cartilage matrix. After deparaffinization and microwave radiation antigen repair, immunohistochemistry was carried out using primary antibodies against Col I (abcam, ab6308), Col II (abcam, ab34712), Col X (abcam, ab182563) and CD31 (abcam, ab182981), an HRP-conjugated anti-rabbit secondary antibody and 3,3′-diaminobenzidine (DAB, brown staining indicates positive immunostaining). The antibody information used in this study was listed in Table S1. Typically, there were six slice samples performed for histological/IHC staining and their quantification in small animal models (mouse ectopic model and rat femoral defect model), with one representative image illustrated. For large animal models (dog segmental radial defect model and dogs mandibular defect model), three slice samples for histological/IHC staining and their quantification, with one representative image presented. All staining slides were captured using a light microscope (Nikon E100, Japan).

2.24. Statistical analyses

All quantitative results were presented as the mean ± SD (standard deviation), and the statistical analysis was conducted using the Graph-Pad Prism software. Prospective power analysis was carried out prior to beginning animal studies by using JMP software. Normal distribution was tested by using Shapiro-Wilk normality test. The groups were compared using a two-tailed Student's t-test, and one-way or two-way analysis of variance (ANOVA) followed by Tukey's post hoc test for multiple comparisons. Significance was accepted at *, #p < 0.05, **, ##p < 0.01, ***, ###p < 0.005 and ****, ####p < 0.0001.

3. Data availability

The sequencing data have been deposited into NCBI sequence read archive (SRA) database under accession number PRJNA881493. Other datasets generated and analyzed during the study can be requested from the corresponding authors.

Ethics approval

All experimental animals were obtained from Shanghai Jiao Tong University School of Agriculture and Biology. The animal experiments were performed in strict accordance with the NIH Guide for the Care and Use of Laboratory Animals, and all procedures were carried out by the Animal Research Committee of Sixth People's Hospital, Shanghai Jiao Tong University School of Medicine (License number: SCXK (Hu) 2017-0007, SYXK (Hu) 2018-0006; Animal research ethics number: NO. DWLL20220602)

CRediT authorship contribution statement

Lili Sun: Conceptualization, Data curation, Formal analysis, Investigation, Methodology, Project administration, Software, Validation, Writing – original draft, Writing – review & editing. **Haoyi Niu:** Conceptualization, Data curation, Formal analysis, Investigation, Methodology, Software. **Yuqiong Wu:** Data curation, Investigation, Methodology, Software. **Shiyan Dong:** Data curation, Formal analysis, Investigation, Methodology. **Xuefeng Li:** Data curation, Investigation, Methodology. **Betty Y.S. Kim:** Investigation, Methodology, Resources. **Changsheng Liu:** Funding acquisition, Project administration, Supervision. **Yifan Ma:** Conceptualization, Data curation, Formal analysis, Investigation, Methodology, Project administration, Software, Supervision, Validation, Visualization, Writing – original draft, Writing – review & editing. **Wen Jiang:** Conceptualization, Project administration, Resources, Supervision, Writing – original draft, Writing – review & editing. **Yuan Yuan:** Conceptualization, Funding acquisition, Investigation, Project administration, Resources, Supervision, Validation, Writing – original draft, Writing – review & editing.

Declaration of competing interest

The authors declare no conflict of interest.

Appendix A. Supplementary data

Supplementary data to this article can be found online at https://doi.org/10.1016/j.bioactmat.2024.01.019.

References

[1] R. Quarto, et al., Repair of large bone defects with the use of autologous bone marrow stromal cells, N. Engl. J. Med. 344 (2001) 385–386.

[2] S.N. Khan, et al., The biology of bone grafting, J. Am. Acad. Orthop. Surg. 13 (2005) 77–86.

[3] E. Roddy, M.R. DeBaun, A. Daoud-Gray, Y.P. Yang, M.J. Gardner, Treatment of critical-sized bone defects: clinical and tissue engineering perspectives, Eur. J. Orthop. Surg. Traumatol. 28 (2018) 351–362.

[4] R.C. Goncalves, A. Banfi, M.B. Oliveira, J.F. Mano, Strategies for re-vascularization and promotion of angiogenesis in trauma and disease, Biomaterials 269 (2021).

[5] L.L. Sun, et al., Recapitulation of in situ endochondral ossification using an injectable hypoxia-mimetic hydrogel, Adv. Funct. Mater. 31 (2021).

[6] J. Shen, et al., Stepwise 3D-spatio-temporal magnesium cationic niche: nanocomposite scaffold mediated microenvironment for modulating intramembranous ossification, Bioact. Mater. 6 (2021) 503–519.

[7] C. Scotti, et al., Engineering of a functional bone organ through endochondral ossification, Proc. Natl. Acad. Sci. U. S. A 110 (2013) 3997–4002.

[8] C. Scotti, et al., Recapitulation of endochondral bone formation using human adult mesenchymal stem cells as a paradigm for developmental engineering, Proc. Natl. Acad. Sci. U. S. A 107 (2010) 7251–7256.

[9] J.M. Jukes, et al., Endochondral bone tissue engineering using embryonic stem cells, Proc. Natl. Acad. Sci. U. S. A 105 (2008) 6840–6845.

[10] D. Lin, et al., Rapid initiation of guided bone regeneration driven by spatiotemporal delivery of IL-8 and BMP-2 from hierarchical MBG-based scaffold, Biomaterials 196 (2019) 122–137.

[11] Y. Liu, et al., Spatiotemporal immunomodulation using biomimetic scaffold promotes endochondral ossification-mediated bone healing, Adv. Sci. 8 (2021) e2100143.

[12] K. Tsuji, et al., BMP2 activity, although dispensable for bone formation, is required for the initiation of fracture healing, Nat. Genet. 38 (2006) 1424–1429.

[13] B.S. Yoon, et al., Bmpr1a and Bmpr1b have overlapping functions and are essential for chondrogenesis in vivo, Proc. Natl. Acad. Sci. U. S. A 102 (2005) 5062–5067.

[14] B. Yan, et al., mTORC1 regulates PTHrP to coordinate chondrocyte growth, proliferation and differentiation, Nat. Commun. 7 (2016) 11151.

[15] R. Amarilio, et al., HIF1alpha regulation of Sox9 is necessary to maintain differentiation of hypoxic prechondrogenic cells during early skeletogenesis, Development 134 (2007) 3917–3928.

[16] S. Hankemeier, et al., Alteration of fracture stability influences chondrogenesis, osteogenesis and immigration of macrophages, J. Orthop. Res. 19 (2001) 531–538.

[17] L. Claes, P. Augat, G. Suger, H.-J. Wilke, Influence of size and stability of the osteotomy gap on the success of fracture healing, J. Orthop. Res. 15 (1997) 577–584.

[18] N. Huebsch, et al., Harnessing traction-mediated manipulation of the cell/matrix interface to control stem-cell fate, Nat. Mater. 9 (2010) 518–526.

[19] S. Moeinzadeh, S.R. Pajoum Shariati, E. Jabbari, Comparative effect of physicomechanical and biomolecular cues on zone-specific chondrogenic differentiation of mesenchymal stem cells, Biomaterials 92 (2016) 57–70.

[20] Y.-Q. Yang, et al., The role of vascular endothelial growth factor in ossification, Int. J. Oral Sci. 4 (2012) 64–68.

[21] L.P. Hatt, K. Thompson, J.A. Helms, M.J. Stoddart, A.R. Armiento, Clinically relevant preclinical animal models for testing novel cranio-maxillofacial bone 3D-printed biomaterials, Clin. Transl. Med. 12 (2022) e690.

[22] A. Petersen, et al., A biomaterial with a channel-like pore architecture induces endochondral healing of bone defects, Nat. Commun. 9 (2018) 4430.

[23] R.E. De La Vega, et al., Efficient healing of large osseous segmental defects using optimized chemically modified messenger RNA encoding BMP-2, Sci. Adv. 8 (2022).

[24] T. Itoh, et al., Repair of ulnar segmental defect by recombinant human bone morphogenetic protein-2 in dogs, J. Vet. Med. Sci. 60 (1998) 451–458.

[25] M.L.E. Faria, et al., Recombinant human bone morphogenetic protein-2 in absorbable collagen sponge enhances bone healing of tibial osteotomies in dogs, Vet. Surg. 36 (2007) 122–131.

[26] C. Maes, G. Carmeliet, E. Schipani, Hypoxia-driven pathways in bone development, regeneration and disease, Nat. Rev. Rheumatol. 8 (2012) 358–366.

[27] J.R. Jones, L.M. Ehrenfried, L.L. Hench, Optimising bioactive glass scaffolds for bone tissue engineering, Biomaterials 27 (2006) 964–973.

[28] H. Niu, et al., Multicellularity-interweaved bone regeneration of BMP-2-loaded scaffold with orchestrated kinetics of resorption and osteogenesis, Biomaterials 216 (2019) 119216.

[29] P.E. Hallaway, J.W. Eaton, S.S. Panter, B.E. Hedlund, Modulation of deferoxamine toxicity and clearance by covalent attachment to biocompatible polymers, Proc. Natl. Acad. Sci. USA 86 (1989) 10108–10112.

[30] Y. Wang, Y.M. Kim, R. Langer, In vivo degradation characteristics of poly(glycerol sebacate), J. Biomed. Mater. Res. 66A (2003) 192–197.

[31] M.I. ul-haq, et al., Design of long circulating nontoxic dendritic polymers for the removal of iron in vivo, ACS Nano 7 (2013) 10704–10716.

[32] Q. Yao, Y. Liu, J. Tao, K.M. Baumgarten, H. Sun, Hypoxia-mimicking nanofibrous scaffolds promote endogenous bone regeneration, ACS Appl. Mater. Interfaces 8 (2016) 32450–32459.

[33] W. Chen, et al., Electrospun fibers improving cellular respiration via mitochondrial protection, Small (2021) e2104012.

[34] X. Zheng, et al., Hypoxia-mimicking 3D bioglass-nanoclay scaffolds promote endogenous bone regeneration, Bioact. Mater. 6 (2021) 3485–3495.

[35] H. Niu, et al., Surface topography regulates osteogenic differentiation of MSCs via crosstalk between FAK/MAPK and ILK/beta-Catenin pathways in a hierarchically porous environment, ACS Biomater. Sci. Eng. 3 (2017) 3161–3175.

[36] Y. Liu, et al., MBG-modified beta-TCP scaffold promotes mesenchymal stem cells adhesion and osteogenic differentiation via a FAK/MAPK signaling pathway, ACS Appl. Mater. Interfaces 9 (2017) 30283–30296.

[37] Z. Wu, et al., Injectable, viscoelastic hydrogel precisely regulates developmental tissue regeneration, Chem. Eng. J. 434 (2021) 133860.

[38] Z. Wu, et al., Core/shell PEGS/HA hybrid nanoparticle via micelle-coordinated mineralization for tumor-specific therapy, ACS Appl. Mater. Interfaces 12 (2020) 12109–12119.

[39] W. Tang, et al., Bioinspired trimodal macro/micro/nano-porous scaffolds loading rhBMP-2 for complete regeneration of critical size bone defect, Acta Biomater. 32 (2016) 309–323.

[40] I. El Bialy, W. Jiskoot, M.R. Nejadnik, Formulation, delivery and stability of bone morphogenetic proteins for effective bone regeneration, Pharm. Res. (N. Y.) 34 (2017) 1152–1170.

[41] Q. Yang, J.L. Jian, S.B. Abramson, X. Huang, Inhibitory effects of iron on bone morphogenetic protein 2-induced osteoblastogenesis, J. Bone Miner. Res. 26 (2011) 1188–1196.

[42] E. Kalay, C. Ermutlu, A.E. Yenigul, U. Yalcinkaya, B. Sarisozen, Effect of bone morphogenic protein-2 and desferoxamine on distraction osteogenesis, Injury 53 (2022) 1854–1857.

[43] R. Stewart, J. Goldstein, A. Eberhardt, G. Chu, S. Gilbert, Increasing vascularity to improve healing of a segmental defect of the rat femur, J. Orthop. Trauma 25 (2011) 472–476.

[44] D. Sha, et al., Development of modified and multifunctional poly(glycerol sebacate) (PGS)-based biomaterials for biomedical applications, Eur. Polym. J. 161 (2021) 110830.

[45] Y. Ma, et al., PEGylated poly(glycerol sebacate)-modified calcium phosphate scaffolds with desirable mechanical behavior and enhanced osteogenic capacity, Acta Biomater. 44 (2016) 110–124.

[46] Z. Wang, et al., Urethane-based low-temperature curing, highly-customized and multifunctional poly(glycerol sebacate)-co-poly(ethylene glycol) copolymers, Acta Biomater. 71 (2018) 279–292.

[47] Y. Ma, et al., Direct three-dimensional printing of a highly customized freestanding hyperelastic bioscaffold for complex craniomaxillofacial reconstruction, Chem. Eng. J. 411 (2021).

[48] Y. Ma, et al., Exosomal mRNAs for angiogenic–osteogenic coupled bone repair, Adv. Sci. 10 (2023) 2302622.

[49] Y. Chai, D. Lin, Y. Ma, Y. Yuan, C. Liu, RhBMP-2 loaded MBG/PEGylated poly (glycerol sebacate) composite scaffolds for rapid bone regeneration, J. Mater. Chem. B 5 (2017) 4633–4647.

[50] S. Stegen, et al., HIF-1alpha promotes glutamine-mediated redox homeostasis and glycogen-dependent bioenergetics to support postimplantation bone cell survival, Cell Metabol. 23 (2016) 265–279.

[51] N. Zhou, et al., HIF-1alpha as a regulator of BMP2-induced chondrogenic differentiation, osteogenic differentiation, and endochondral ossification in stem cells, Cell. Physiol. Biochem. 36 (2015) 44–60.

[52] T.F. Day, X. Guo, L. Garrett-Beal, Y. Yang, Wnt/beta-catenin signaling in mesenchymal progenitors controls osteoblast and chondrocyte differentiation during vertebrate skeletogenesis, Dev. Cell 8 (2005) 739–750.

[53] J.A. Stefater, et al., Regulation of angiogenesis by a non-canonical Wnt-Flt1 pathway in myeloid cells, Nature 474 (2011) 511–515.

[54] F.X. Long, et al., Ihh signaling is directly required for the osteoblast lineage in the endochondral skeleton, Development 131 (2004) 1309–1318.

[55] B. St-Jacques, M. Hammerschmidt, A.P. McMahon, Indian hedgehog signaling regulates proliferation and differentiation of chondrocytes and is essential for bone formation, Genes Dev. 13 (1999) 2072–2086.

[56] J.B. Regard, et al., Wnt/beta-catenin signaling is differentially regulated by Galpha proteins and contributes to fibrous dysplasia, Proc. Natl. Acad. Sci. U. S. A 108 (2011) 20101–20106.

[57] M. Kisiel, et al., Critical assessment of rhBMP-2 mediated bone induction: an in vitro and in vivo evaluation, J. Contr. Release 162 (2012) 646–653.

[58] W. Zhang, et al., Strontium attenuates rhBMP-2-induced osteogenic differentiation via formation of Sr-rhBMP-2 complex and suppression of Smad-dependent signaling pathway, Acta Biomater. 33 (2016) 290–300.

[59] R. Fu, C.Q. Liu, Y.X. Yan, Q.F. Li, R.L. Huang, Bone defect reconstruction via endochondral ossification: a developmental engineering strategy, J. Tissue Eng. 12 (2021).

[60] J.N. Zara, et al., High doses of bone morphogenetic protein 2 induce structurally abnormal bone and inflammation in vivo, Tissue Eng. 17 (2011) 1389–1399.

[61] E.J. Carragee, E.L. Hurwitz, B.K. Weiner, A critical review of recombinant human bone morphogenetic protein-2 trials in spinal surgery: emerging safety concerns and lessons learned, Spine J. 11 (2011) 471–491.

[62] F.E. Freeman, et al., 3D bioprinting spatiotemporally defined patterns of growth factors to tightly control tissue regeneration, Sci. Adv. 6 (2020).

[63] M. Sarem, M. Heizmann, A. Barbero, I. Martin, V.P. Shastri, Hyperstimulation of CaSR in human MSCs by biomimetic apatite inhibits endochondral ossification via temporal down-regulation of PTH1R, Proc. Natl. Acad. Sci. U. S. A 115 (2018) E6135–E6144.

[64] S.W. Jin, K.B. Sim, S.D. Kim, Development and growth of the normal cranial vault : an embryologic review, J Korean Neurosurg Soc 59 (2016) 192–196.

[65] S.Y. Park, K.H. Kim, S. Kim, Y.M. Lee, Y.J. Seol, BMP-2 gene delivery-based bone regeneration in dentistry, Pharmaceutics 11 (2019).

[66] W.F. McKay, S.M. Peckham, J.M. Badura, A comprehensive clinical review of recombinant human bone morphogenetic protein-2 (INFUSE (R) Bone Graft), Int. Orthop. 31 (2007) 729–734.

[67] M.L. Faria, et al., Recombinant human bone morphogenetic protein-2 in absorbable collagen sponge enhances bone healing of tibial osteotomies in dogs, Vet. Surg. 36 (2007) 122–131.

[68] R. Xu, et al., Galphas signaling controls intramembranous ossification during cranial bone development by regulating both Hedgehog and Wnt/beta-catenin signaling, Bone Res. 6 (2018) 33.

[69] B. St-Jacques, M. Hammerschmidt, A.P. McMahon, Indian hedgehog signaling regulates proliferation and differentiation of chondrocytes and is essential for bone formation (vol 13, pg 2072, 1999), Genes Dev. 13 (1999) 2617, 2617.

[70] F. Long, U.I. Chung, H. Kronenberg, A. McMahon, Ihh signaling is directly required for the osteoblast lineage in the endochondral skeleton, Faseb. J. 18 (2004) A398–A399.

[71] G.J. Wang, et al., Design and compressive behavior of controllable irregular porous scaffolds: based on voronoi-tessellation and for additive manufacturing, ACS Biomater. Sci. Eng. 4 (2018) 719–727.

[72] Q. Zhang, et al., Effects of the fibrous topography-mediated macrophage phenotype transition on the recruitment of mesenchymal stem cells: an in vivo study, Biomaterials 149 (2017) 77–87.

[73] J.A. McGovern, M. Griffin, D.W. Hutmacher, Animal models for bone tissue engineering and modelling disease, Dis. Model. Mech. 11 (2018).

[74] A.M. Hoffman, S.W. Dow, Concise review: stem cell trials using companion animal disease models, Stem Cell. 34 (2016) 1709–1729.

[75] Karl H. Kraus, H.W.A.K.M.S.M.H.W.C.H.C.A.K.-H.S.B., Critically sized osteo-periosteal femoral defects: a dog model, J. Invest. Surg. 12 (1999) 115–124.